UPCommons

Portal del coneixement obert de la UPC

http://upcommons.upc.edu/e-prints

Thermo-mechanical parametric analysis of packed-bed thermocline energy storage tanks

Ignacio González[1], Carlos David Pérez-Segarra[1], Oriol Lehmkuhl[1], Santiago Torras[1], Assensi Oliva[1,*]

[a]*Heat and Mass Transfer Technological Center (CTTC), Universitat Politècnica de Catalunya - BarcelonaTech (UPC), ESEIAAT, Carrer de Colom 11, 08222, Terrassa (Barcelona), Spain*

Abstract

A packed-bed thermocline tank represents a proved cheaper thermal energy storage for concentrated solar power plants compared with the commonly-built two-tank system. However, its implementation has been stopped mainly due to the vessel's thermal ratcheting concern, which would compromise its structural integrity. In order to have a better understanding of the commercial viability of thermocline approach, regarding energetic effectiveness and structural reliability, a new numerical simulation platform has been developed. The model dynamically solves and couples all the significant components of the subsystem, being able to evaluate its thermal and mechanical response over plant normal operation. The filler material is considered as a cohesionless bulk solid with thermal expansion. For the stresses on the tank wall the general thermoelastic theory is used. First, the numerical model is validated with the Solar One thermocline case, and then a parametric analysis is carried out by settling this storage technology in two real plants with a temperature rise of 100 ºC and 275 ºC. The numerical results show a better storage performance together with the lowest temperature difference, but both options achieve suitable structural factors of safety with a proper design.

Keywords: thermal energy storage, thermocline, concentrated solar power, thermal ratcheting, numerical modeling

---

[*]Corresponding author.
Email address: cttc@cttc.upc.edu (Assensi Oliva)

1. Introduction

Concentrated solar power (CSP) plants have become one of the most reliable promises for a sustainable energy future. They are able to transform the solar radiation into electricity by means of a collector system and a thermodynamic power cycle. The collector involves a set of reflectors that focuses the sunlight on a point (power tower, parabolic dish), or along a line (parabolic through, Fresnel). A heat transfer fluid (HTF) is pumped to the reflectors focal region so that it absorbs the thermal energy. In many applications, this hot fluid works as the hot source within the power cycle by evaporating water. Eventually, the resulting steam moves a turbine and the electrical generator.

As a result of the day/night cycle and the weather, a thermal energy storage (TES) is essential, which is able to match supply and demand of energy in order to be commercially viable. This system collects the surplus thermal energy and provides it when there is not enough solar radiation to cover all the demand. The current standard storage for CSP is the two-tank molten salt TES in which there is a separate tank for the hot and cold fluid. Since its associated investment and operational costs are relatively high, different cheaper approaches have been considered.

In this sense, containing both fluids in a single thermocline storage tank is becoming a promising alternative as can be observed in the literature [1, 2, 3]. The common design is a dual-media vessel containing the HTF and an inert granulate material, preferably quartzite rock and silica sand [4], which works as a porous medium. It is based on the principle of buoyancy stratification to separate hot and cold fluid; the former with a lower density at the top, and the latter at the bottom. Thus, a charging process (i.e. heating) is carried out by introducing the HTF from the upper tank section and a discharging process (i.e. cooling) from the base. The main benefit of the filler material is the reduction of higher-cost fluid required, since the solid is acting as the major sensible heat storage medium. This, together with the use of one tank instead of two, is translated in costs savings of approximately 33% compared with the two-tank molten salt approach [5, 6].

Despite its proven potential, there is still a critical concern that has stopped it from being implemented in commercial plants. It refers to thermal ratcheting, a phenomenon that might compromise the structural integrity of the system [7, 5, 8]. It may occur when a tank filled with particulate solids is cyclically heated and cooled. As long as the wall has a greater thermal

expansion than the filler material, a radial gap is generated between both during heating, allowing the cohesionless particles to settle lower to fill it. When temperature drops, the tank is unable to contract completely, resulting in thermal stresses that may cause plastic deformation. If the strain hardening cannot prevent the same process in the next heating and cooling cycles, the tank wall will be slowly ratcheted outward until it fails.

Some technological solutions have already been suggested in order to elude the thermal ratcheting matter. A composite wall for the vessel has been proposed by [8]. It settles an insulation layer between the inside and the metal shell, to minimize the wall temperature variation and consequently, the potential of ratcheting. A buried concrete tank with a truncated cone shape for guiding the rocks upwards during thermal expansion and, therefore, reducing lateral pressure on the walls, has been tested and modeled [9]. Air worked as HTF and no liquid option was contemplated. Another concept removes all the solid filler material, obtaining a single-media thermocline tank with fluid only [10]. Even though convective mixing flows are significant without the porous media, the thermal diffusivity lessens, so it can achieve a slightly better thermal function. A structured packed thermocline tank can also be considered as a viable proposal [11, 12, 13]. Different arrangements of structured material can be chosen to replace the packed aggregated bed so as to avoid solid filler settlement. The principal disadvantage of all these alternatives compared with the original thermocline rests on economics.

Although there have been an extensive research regarding heat transfer and storage performance of thermocline tanks [6, 14, 15, 16, 17], few works have carried out a mechanical analysis that addresses the ratcheting issue. The design of the experimental thermocline system of Solar One Pilot Plant [18, 19] imposed a high yield strength material for the tank wall in order to avoid any plastic deformation. It was developed considering the active load of the inner gravel and its differential expansion with the shell. Only a particular stress state was evaluated: the cooldown from maximum temperature to ambient temperature with an assumed rigid filler. During the 5-year performance of these facilities, no evidence of thermal ratcheting was appreciated and some measures of tank wall hoop stress were taken [7]. Unfortunately, they showed great uncertainty and no conclusion was reached.

The subsequent investigations have been limited to numerical modeling. The mentioned Solar One case has been reproduced using a static stress-strain finite element analysis with two states of maximum and minimum operating temperatures [8, 20]. The solid was simplified to be a cohesionless

3

rigid medium without weight or thermal expansion. Filler solid and shell have been analyzed more precisely considering elastoplastic numerical models in [21]. Preliminary results showed that bed physical properties are a key aspect to overcome ratchet failure. For this reason, experimental measures of these bed properties have been reported [22]. In [23], the dynamic evolution of tank wall stresses during a charge-discharge cycle was discussed but it did not take into account the thermal expansion of the particles.

This paper presents an original validated numerical model which is able to evaluate the energetic and mechanical response of these storage tanks during a CSP plant normal operation. Compared with previous studies, this includes the thermal interaction between the principal components of the subsystem: particulate solid, fluid, shell, insulation, ullage, ground and environment. In this manner, the simulated plant and storage face real operating and weather conditions while performing an exhaustive thermal loss calculation. The structural analysis is improved by means of a complete model for the filler material, which considers temperature expansion and bulk solid mechanical behaviour, and a generalized thermoelastic model for the walls.

The whole platform is employed to simulate different thermocline configurations within two different CSP plants that are currently working with a two-tank molten salt storage subsystem, Andasol and Gemasolar. First, tanks are properly sized for each scenario, and then a parametric study is carried out in order to test the storage performance and the risk of ratchet failure throughout normal operating conditions. In the authors' opinion, the combination of such an advanced complete model with this kind of analysis has still not been presented in the literature. Consequently, a better awareness of the viability of packed-bed thermocline storage for solar plants is provided.

2. Mathematical and numerical model

All components whose physics are solved and coupled in the present dual-media thermocline model are outlined in Figure 1. The subsystem is basically a tank filled with fluid and a bulk solid material. The walls are made up of metal rings with varying thickness. In order to minimize thermal losses, roof and sides are covered with an insulation blanket with a metal weather cover. There is an ullage space available above the fluid and bed to accommodate substance thermal expansion and to keep a non-hazardous inert gas. The ground consists of different layers of foundation and soil. When charging, hot
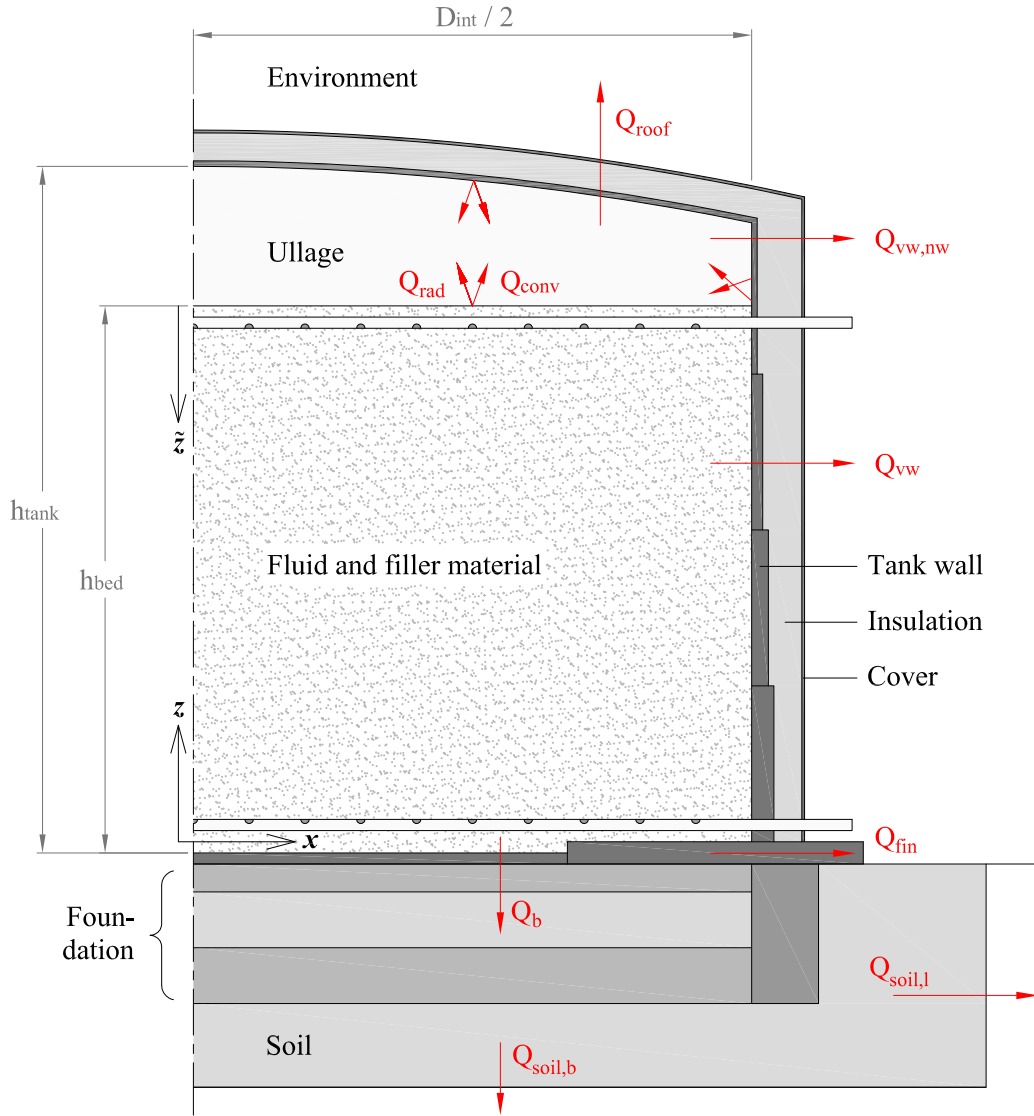
4

Figure 1: Elements of the thermocline storage tank and their boundary conditions.

fluid at T_{hot} is introduced through a manifold into the top of the tank and is drawn from a lower manifold, warming up the filler material. During the discharge process, cold fluid at T_{cold} is pumped upwards, recovering through its way up the heat from the porous bed.

The coupling of all these elements considering the transient thermal and mechanical loads has been implemented within the existing NEST platform [24, 25]. It is a parallel computing code based on a modular object oriented methodology. The individual solvers of each part are coupled explicitely, i.e. they use the boundary conditions defined by the linked elements in the previous time step. The mathematical models of the environment, ground, ullage and insulation are described in [25] and [26]. The packed-bed and shell physics as well as the subsystem management are described hereinafter.

2.1. Storage management

The storage tank functioning relies on three variables: radiation availability, plant electric demand and stop-restart criteria for both charge and discharge processes. To take into account the whole power plant, a simplified replicable model is proposed. It consists of three main subsystems: a solar field (SF), a TES and a power block (PB), as it is sketched in Figure 2. It is supposed to have constant firm capacity $\dot{W}_{EG}$. Thus, the thermal energy required for the hot source of the thermodynamic cycle is also constant,

$$\dot{Q}_{\mathrm{PB}} = \dot{W}_{\mathrm{EG}}/\eta_{\mathrm{PB}} \tag{1}$$

where the thermal efficiency of the PB is given by η_{PB}. In the solar field the heat absorbed by the fluid from the sun is proportional to the direct normal irradiance DNI, the collector area A_{SF} and the solar field collecting efficiency η_{SF}:

$$\dot{Q}_{\mathrm{SF}} = DNI \cdot A_{\mathrm{SF}} \cdot \eta_{\mathrm{SF}} \tag{2}$$

Having defined the thermal energy the HTF should exchange in both subsystems, the mass flows are to be found with the following enthalpic balances:

$$\dot{Q}_{\mathrm{SF}} = \dot{m}_{\mathrm{SF}} \cdot \bar{C}_{p,f} \cdot \left(T_{\mathrm{SF}}^{out} - T_{\mathrm{SF}}^{in}\right) \tag{3}$$

$$\dot{Q}_{\mathrm{PB}} = \dot{m}_{\mathrm{PB}} \cdot \bar{C}_{p,f} \cdot \left(T_{\mathrm{PB}}^{in} - T_{\mathrm{PB}}^{out}\right) \tag{4}$$

At this point, if $\dot{m}_{\mathrm{SF}}$ is larger than $\dot{m}_{\mathrm{PB}}$, the storage will charge with a mass flow of $\dot{m}_C = \dot{m}_{\mathrm{SF}} - \dot{m}_{\mathrm{PB}}$. Otherwise, discharge will be set with $\dot{m}_D =$
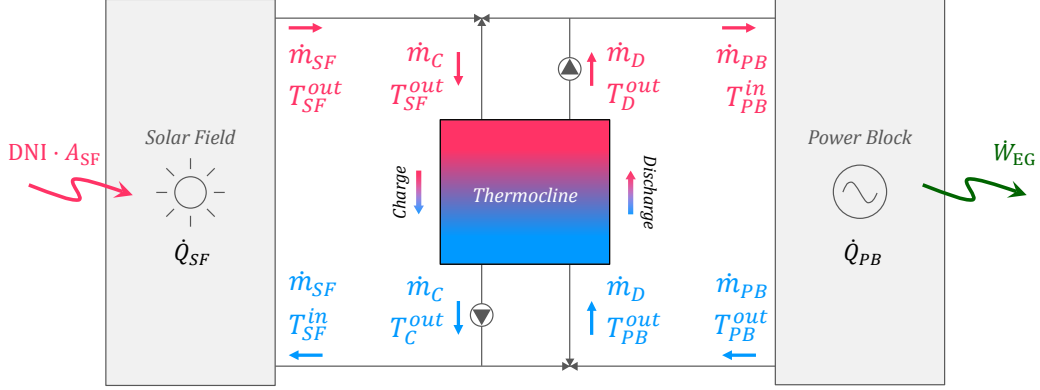
Figure 2: Plant diagram with a direct storage system scheme.

$\dot{m}_{\mathrm{PB}} - \dot{m}_{\mathrm{SF}}$. The resulting mixture between outflows from the subsystem SF or PB and the storage gives rise to the updated inlet temperatures (see [Figure 2](#)).

$$T_{\mathrm{SF}}^{in} = \left(\dot{m}_{\mathrm{PB}} T_{\mathrm{PB}}^{out} + \dot{m}_{C} T_{C}^{out} \right) / \dot{m}_{\mathrm{SF}} \tag{5}$$

$$T_{\mathrm{PB}}^{in} = \left(\dot{m}_{\mathrm{SF}} T_{\mathrm{SF}}^{out} + \dot{m}_{D} T_{D}^{out} \right) / \dot{m}_{\mathrm{PB}} \tag{6}$$

where T_{SF}^{out} and T_{PB}^{out} are kept invariable controlling the mass flows and equal to T_{hot} and T_{cold}, respectively. The inlet temperatures for the solar field and the power block are used to decide whether the TES process (charge or discharge) can continue or should be stopped. Since there is a thermal gradient inside the tank, the output temperature is expected to be higher than T_{cold} at the end of charge and less than T_{hot} at the end of discharge. In this work, both receiver and generation subsystems are supposed to accept inlet temperatures that deviates ΔT_{CO} from their design magnitude. Bearing this in mind, the cut-off temperature for charging will be $T_{cold} + \Delta T_{CO}$, while it will be $T_{hot} - \Delta T_{CO}$ for discharging.

Furthermore, to avoid several charge and discharge being started and stopped in small time intervals, further thresholds have been defined for restarting the processes. In this sense, and considering a temperature restart tolerance of ΔT_R which is smaller than ΔT_{CO}, discharge does not start if the temperature at the top of the tank is lower than $T_{hot} - \Delta T_R$, while the charge if the temperature at the bottom is higher than $T_{cold} + \Delta T_R$.

2.2. Tank inner substances

The model presented in [17] is used. Mass, momentum and energy conservation equations have to be solved in order to be able to simulate the thermal behaviour of the packed bed. These equations are discretized using the Finite Volume Method (FVM) and assuming one-dimensionality in the fluid flow (axial direction of the cylindrical column) and in the heat transfer inside particles (radial direction of spherical shaped pebbles). Thus, only a single representative particle needs to be simulated in each tank section. The tank is divided into N_z cylindrical sections of height Δz_i, and the filler particle into N_r spherical volumes.

For the HTF going through the porous bed, the semi-discrete energy conservation equation in the ith tank section ($i = 1 \dots N_z$) results in:

$$
\begin{aligned}
\rho_f \epsilon_i V_i C_{p,f} \frac{\partial T_{i,f}}{\partial t} = {} & A_t \left(k_{eff} \frac{\partial T_f}{\partial z} \right) \bigg|_{i-1/2}^{i+1/2} \\
& - \dot{m} C_{p,f} \left(T_{i+1/2,f} - T_{i-1/2,f} \right) \\
& - n_{s,i} \frac{T_{i,f} - T_{i.0}}{R_{conv,i}} \\
& - U_{TC-Sh} A_{w,i} \left(T_{i,f} - T_{i,Sh} \right)
\end{aligned}
\tag{7}
$$

where $n_{s,i}$ is the number of filler particles, $T_{i,0}$ is the temperature on the surface of the particles, and ϵ_i is the volume liquid fraction (porosity) that results from the ith bed composition. In the advective term (second on the right hand side) the fluid is assumed to be coming from section $i - 1$ and going to section $i + 1$. The calculation of the thermal resistance R_{conv} due to convection between the HTF and the filler material requires the fluid-to-bed Nusselt number, which is calculated using the correlation obtained from [27]. Consequently, the effective thermal conductivity, k_{eff}, takes into account the effects of molecular diffusion and thermal dispersion.

The energy balance for the inner nodes ($j = 1 \dots N_r$ from outside to inside) of the filler material remains:

$$
\rho_s V_{i,j} C_{p,s} \frac{\partial T_{i,j}}{\partial t} = \left(k_s A \frac{\partial T}{\partial r} \right)_{i,j-1/2} - \left(k_s A \frac{\partial T}{\partial r} \right)_{i,j+1/2}
\tag{8}
$$

where the enthalpy is evaluated by means of the specific heat capacity $C_{p,s}$. For the boundary node ($j = 0$), which is in contact with the fluid, the

8

equation, neglecting thermal conduction between different particles, becomes

$$\rho_s V_{i,0} C_{p,s} \frac{\partial T_{i,0}}{\partial t} = \frac{T_{f,i} - T_{i,0}}{R_{conv,i}} - \left(k_s A \frac{\partial T}{\partial r} \right)_{i,1/2} \tag{9}$$

Regarding the discretization, the diffusive terms in equations 7-9 have been approximated by a 2nd order central difference spatial scheme and a fully implicit temporal integration. The convective term is time-integrated using a fully explicit upwind scheme.

For further details of the model and the discretization employed see [17].

2.3. Tank wall

Once the packed-bed has been solved for a given instant by following the description of the previous section, the temperature field on the shell is calculated. The stress-strain state of the tank wall can then be found taking into account the thermal load and the pressure of the inner substances.

A linear thermoelastic solid model is applied for the tank walls. The linear model is used owing to the small strains the shell is subjected to. It is elastic because it is enough to establish if yield point has been reached, i.e. if solid undergoes non-reversible plastic behaviour. This kind of solid is governed by the conservation laws for energy and momentum, whose lagrangian form integrated over a control volume V is:

$$\int_V \rho C_p \frac{\partial T}{\partial t} dV = \oint_A k \nabla T \cdot \boldsymbol{n} dA - \int_V \alpha \left(2\mu + 3\lambda \right) T \mathrm{tr}\left(\dot{\boldsymbol{\varepsilon}} \right) dV \tag{10}$$

$$\int_V \rho \frac{\partial \boldsymbol{v}}{\partial t} dV = \oint_A \boldsymbol{\sigma} \cdot \boldsymbol{n} dA + \int_V \rho \boldsymbol{f} dV \tag{11}$$

where the energy source term depending on the strain rate $\dot{\boldsymbol{\varepsilon}}$ is negligible due to the slow change in the boundary conditions. The body force $\boldsymbol{f}$ has been replaced by the gravitational acceleration in the vertical direction in order to add the structure's own weight. The linear constitutive equation that specifies the relation between stress $\boldsymbol{\sigma}$, strain $\boldsymbol{\varepsilon}$ and temperature is:

$$\boldsymbol{\sigma} = 2\mu\boldsymbol{\varepsilon} + \lambda \mathrm{tr}\left(\boldsymbol{\varepsilon} \right) \boldsymbol{1} - \alpha \left(2\mu + 3\lambda \right) \left(T - T_0 \right) \boldsymbol{1} \tag{12}$$

where T_0 is the reference temperature with no thermal strain (in this case the ambient temperature), α is the thermal expansion coefficient and μ and λ are the Lamé's coefficients, dependent only on Young's modulus of elasticity E and Poisson's ratio ν.

The infinitesimal strain is related at the same time with the displacements $\boldsymbol{u}$ through the compatibility equations,

$$\boldsymbol{\varepsilon} = \frac{1}{2}\left[\nabla\boldsymbol{u} + (\nabla\boldsymbol{u})^T\right] \tag{13}$$

where the components $\varepsilon_{r\theta}$ and $\varepsilon_{\theta z}$ are zero, as well as $\sigma_{r\theta}$ and $\sigma_{\theta z}$, due to axisymmetric boundary conditions.

The equations are also discretized using the FVM but on a three-dimensional mesh with axisymmetric boundary conditions. Transient evaluation of stress-strain is calculated using incremental formulation. A detailed explanation of the formulation, accuracy and efficiency of FVM with elasticity is available in [28, 29].

2.3.1. Mechanical boundary conditions

In terms of the stress-strain calculation, the vessel geometry is simplified to a cylinder. There is a Dirichlet zero boundary condition in the vertical displacement at the bottom surface and a traction boundary condition at the other surfaces. This traction is nonzero only on the top surface and on the inner sidewall. The load on the top of the cylinder is the weight of the roof. On the inner wall surface there is the fluid pressure, p_f, and bed pressure, p_s,

$$p\left(\tilde{z}\right) = p_f\left(\tilde{z}\right) + p_s\left(\tilde{z}\right) \tag{14}$$

where $\tilde{z}$ is the depth of the fluid column.

The fluid pressure is mainly the sum of the ullage pressure plus the fluid hydrostatic pressure, since slow flow velocity makes its pressure loss negligible.

$$p_f\left(\tilde{z}\right) = p_{ullage} + \rho_f g\tilde{z} \tag{15}$$

The particulate solid load is measured through the Rankine active pressure [19]. It is based on the equilibrium of a bulk solid element like the one in Figure 3, and defines a ratio between vertical, p_v, and lateral pressure, p_s. Compared with Jansen's theory, Rankine's does not consider any wall-filler friction ($\tau = 0$). This leads to a more conservative model which is appropriate for bunker-shape vessels like the thermocline ones [30]. Knowing the zero value of p_v at the bed free surface ($i = N_z$), the pressure at the bottom can be sequentially found in a discretized manner:

$$p_{v,i-1/2} = p_{v,i+1/2} + \rho_{buo,i}g\Delta z \tag{16}$$
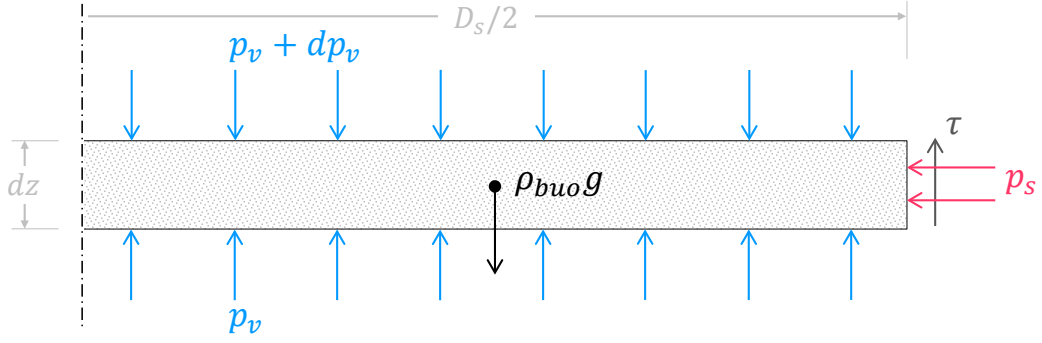
$$p_{v,i} = \frac{p_{v,i+1/2} + p_{v,i-1/2}}{2} \tag{17}$$

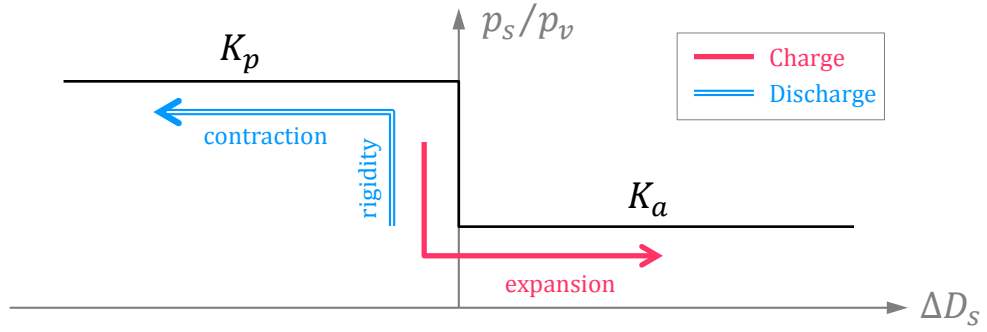Figure 3: Force diagram of a cylindrical slice from the bulk solid.

Figure 4: Bulk solid response using a rigid-perfectly plastic model.

where ρ_{buo} is the buoyant density of the solid in the fluid,

$$\rho_{buo,i} = (1 - \epsilon_i)(\rho_s - \rho_f) \tag{18}$$

The ratio K_a between lateral and vertical pressure ($p_{s,i} = K_a p_{v,i}$), according to Rankine's theory, is given by:

$$K_a = \frac{1 - \sin(\phi)}{1 + \sin(\phi)} \tag{19}$$

where ϕ is the angle of internal friction of the contained material.

The thermal load comes from the different thermal expansion between the bed and the tank wall [19]. When the temperature increases, the tank expands more than the filler, giving rise to a gap. The solid medium, assumed cohesionless, slumps downwards filling the gap. When the temperature decreases, the tank can only contract to the new dimension of the cooled inner solid,

$$D_{i,s}^{n+1} = D_{i,s}^n \left[1 + \alpha_s \left(T_i^{n+1} - T_i^n\right)\right] \tag{20}$$

where α_s is the solid thermal expansion coefficient, $D_{i,s}^{n+1}$ is the bed diameter at the end of a time interval (Δt), which moves from n to $n + 1$ iteration.

The solid is preventing the total contraction of the wall by exerting a lateral load higher than the active pressure. Therefore, the wall strained radius is always forced to not be smaller than the bed one. When this limit is reached in one tank section i, its inner radial boundary condition changes from traction to Dirichlet, with the magnitude of the filler strain.

However, there is a maximum lateral resistance that a given soil can offer to a retaining wall that is pushing towards it. The soil will fail by shearing as soon as a maximum pressure known as passive pressure is reached [31]. Considering the filler material as a loose cohesionless soil, it can be simplified to a rigid-perfectly plastic material with a passive pressure limit [32]. As a result, p_s is constrained to be less than or equal to the passive pressure. To evaluate this passive pressure, the ratio K_p is used following the next expressions [33]:

$$K_p = 1/K_a \tag{21}$$
$$p_{s,i}^{\max} = K_p p_{v,i} \tag{22}$$

In Figure 4, the response of the filler material under the system thermal expansion is summarized. During cooling, the tank wall can only reduce its

radius to the new diminished bed radius; the solid lateral pressure starts increasing, but its radius does not change. If cooling continues and the maximum passive pressure is reached, the aggregated solid fails by shearing and starts to reduce its radius. When heating, due to tank-filler differential expansion, the particles are able to freely expand, and lateral pressure can fall down to the active value. Therefore, a day-periodic load history of relaxation-traction stress is expected in the tank over its service life.

2.3.2. Structural factors of safety

As it has been stated, filler pressure and, consequently, tank wall stress grow during discharge. If wall stress rises above yield strength, all the thermal strain drop will not be able to change to elastic strain and a plastic deformation will appear. Since this tensile plastic strain cannot be removed, next heating strain will result in an increase of the total strain, i.e. the shell radius will enlarge. Then, rocks will settle down in the new gap which has been opened and the process will start again. Yielding is set in each cooling and a radius increment in each heating. In the end, successive plastic deformation will induce cracks and probably a ratcheting collapse.

If the equivalent stress does not exceed yield strength, the strain diminished by temperature when cooling will be compensated completely by elasticity and vice versa when heating, without deforming plastically. Predicting yield by comparing the equivalent tensile stress with the material yield strength is formally known as the von Mises yield criterion, and is useful for multidimensional problems with ductile materials. The corresponding factor of safety against yielding is defined as:

$$FoS_{static} = \frac{\sigma_y}{\sigma_{eq}} \tag{23}$$

where σ_y stands for yield strength.

If this factor is maintained above one in all the tank geometry over its whole service life, no thermal ratcheting will appear. It has been referred to as "static" since it is defined only by the worst situation, the one in all the tank and in all the operation time in which the lowest value is reached. As a result, the factor is possibly too conservative. The structure may be plastically deformed only on a specific day, but this fact is not dangerous in terms of thermal ratcheting since ratcheting requires repeated plastic deformation.

Consequently, in order to take into account the dynamic cyclic behaviour of the system (daily relaxation-traction stress), another factor of safety has
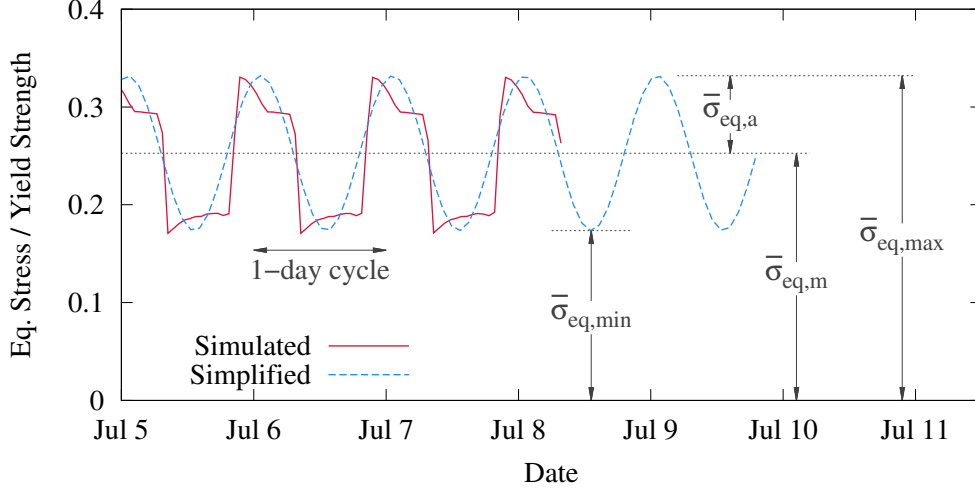
Figure 5: Load history of reference case $\mathcal{G}$ tank (defined in section 4) at h = 6 m with the nomenclature for the simplified constant amplitude cyclic loading.

been defined. It is evaluated similarly to the yield factor of safety used in the Goodman relation for classical S-N (stress-life) fatigue analysis [34, 35] (Figure 5). The resulting formulation contains the daily averaged minimum and maximum equivalent stresses.

$$FoS_{dynamic} = \frac{\sigma_y - \bar{\sigma}_{eq,\min}}{\bar{\sigma}_{eq,\max} - \bar{\sigma}_{eq,\min}} \tag{24}$$

In this manner, if there is no stress oscillation ($\bar{\sigma}_{eq,\min} = \bar{\sigma}_{eq,\max}$), a high safety factor will be obtained. But if there is oscillation and the maximum stress repeatedly approaches the yield limit, then the factor of safety will drop.

3. Model validation

3.1. Case definition

The experimental non-commercial 170 MWht thermocline system of Solar One Pilot Plant is taken as a sample of performance of these storage tanks [7, 18, 19]. Although this first large-scale thermocline tank differs from what today is projected, e.g. in the use of molten salts as HTF in place of

14

hydrocarbon oil, the thermo-mechanical behaviour is qualitatively identical. Furthermore, since the case has been experimentally tested (bed temperature and wall stress), it can be used to validate the developed mathematical model.

Keeping in mind the validation purpose of this case, only two days of operation will be simulated. The first one, with an initial bed temperature of T_{cold} at 9 am, represents the system start-up and has the major variations in stress-strain physics. The second is a good example of the normal tank performance, but still with a high temperature stratification.

Solar One thermocline tank is a cylindrical vessel 18.2 m in inner diameter and 14 m high, composed of carbon manganese-silicon steel plates (A537 Class 2), and covered by 0.229 m of fiberglass insulation. The steel wall plate thickness decreases discretely from bottom to top as follows: 0.0286, 0.019, 0.0156, 0.0095, 0.0079 and 0.019 m. A total of six plates: the one below, with a height of 1.8 m, is followed by four plates 2.86 m high, and the last one is 0.38 m.

Inside an oil known as Caloria HT-43 works as HTF. The resulting fillerbed composition is, according to [7], from bottom to top: 0.66 m of sand-only region (porosity $\epsilon = 0.4$ and effective particle diameter $d_s = 0.002$ m), 1.1 m of rocks ($\epsilon = 0.4$ and $d_s = 0.05$ m), 10.5 m of quartzite rock and sand mixture ($\epsilon = 0.22$ and $d_s = 0.0046$ m) and 0.5 m of rocks again. The ullage is filled by nitrogen pressurized to 2240 Pa above atmospheric pressure.

Physical properties for the fluid, the particulate solid and the steel are presented in Table 1. Temperature dependent physical properties of steel are tabulated in the original source and are treated as piecewise linear functions in the code. Data for the insulation material have been taken from [7].

In order to copy the actual working conditions of the tank as much as possible, in this specific case the inlet variables are not managed by equations 1-6, but they are directly imposed: temperature, mass flow and timing. Regarding the modes of operation reported in [38], the oil worked from a hot temperature of 304 ºC to a cold one of 204 ºC. The oil mass flow pumped into the tank was highly variable and difficult to measure. For this study, a constant average flow rate of 70 kg/s, both for charge and discharge, is considered. However, since the bed starts from a uniform temperature of T_{cold}, the mass flow is increased to 90 kg/s for the start-up charge in order to warm the system completely. Every charge-discharge-standby cycle lasts 1 day; charge starts at 9 am and discharge at 6 pm. The processes are stopped taking into account a cut-off temperature increment ΔT_{CO} of 4 ºC.
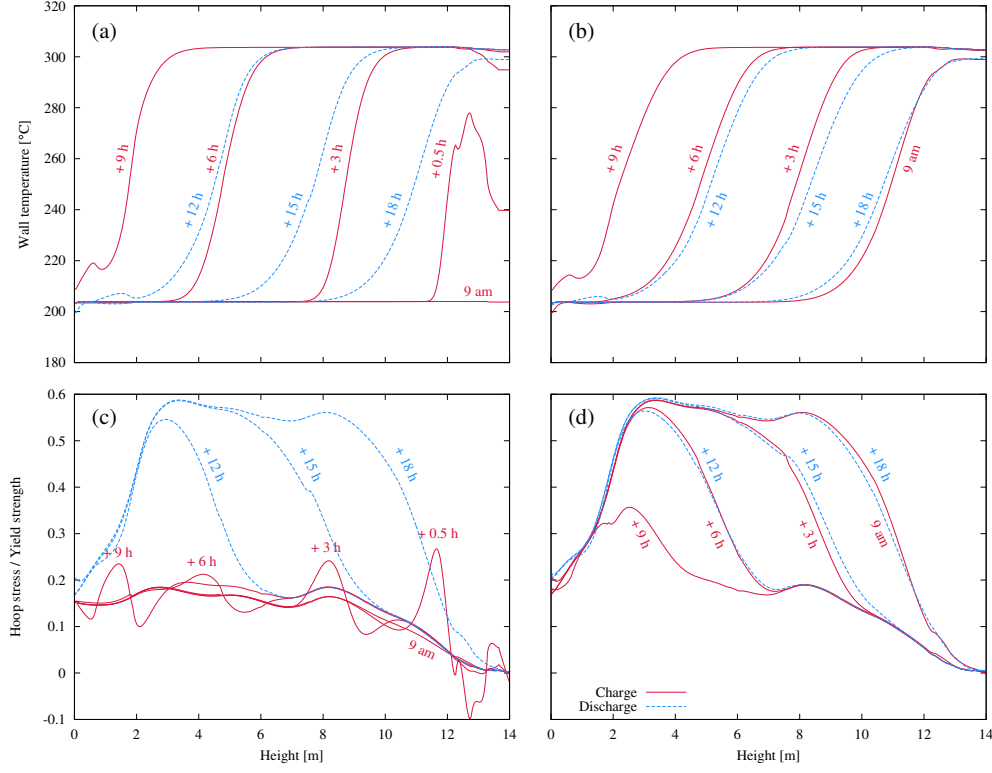
Figure 6: Summary of the Solar One thermocline start-up. Tank wall temperature during the first (a) and the second day (b); and tank wall hoop stress during the first (c) and the second day (d). Profiles belonging to charge (solid lines) and discharge (dashed lines) processes.

Bed and fluid have been discretized axially in 500 control volumes, and the automatically fitted time step [39] is around 4 s. The tank shell element for the thermoelastic problem has been divided axially in 400 sections, and radially in 3 sections. Its physics does not require such a small time increment, thus one of 900 s is used.

3.2. Results

A summary of the most relevant results for the Solar One storage tank during the start-up is presented in Figure 6. As a result of the external insulation, wall temperature is always very close to the fluid temperature, and it is not really affected by the environment variable conditions. The major difference between bed and wall temperatures is appreciated near the

ground, at around 1 m high, when the tank is fully charged (Figure 6 (a) "+ 9 h" curve). It is due to the fillerbed composition and the derived oil-shell convection coefficient, which is changing abruptly from sand to rock layer (from 0.002 to 0.05 m in d_s).

Besides, the thermocline degradation throughout day-cycles is also noticeable. The initial condition in the first charge process (at 9 am) is a uniform cold temperature along the tank. For the next cycles, the initial condition of the bed is not a uniform temperature anymore, but a gradient temperature resulting from the previous discharge process and the requirements imposed on the outgoing fluid temperature. Since the difference between the incoming fluid temperature and that of the filler material is lower than in the 1st charge process, the thermal gradient and hence the heat transfer rate are also lower in following cycles. Therefore, during the consecutive charge-discharge cycles, the thermal gradient tends to get "flattened" until a periodic steady state is reached. Due to this thermocline degradation, the stored energy in the periodic state is lower than that of the initial cycles, and so is the operation time, since outlet thresholds are reached earlier.

Figure 6 also includes the shell hoop stress $\sigma_{\theta\theta}$ resulting mainly from the weight of the inner substances and from bed-shell differential thermal expansion. Any pressure applied by inner substances generates a radial stress σ_{rr} that varies from the value of this pressure p on the interior surface, to p_{atm} outside. As simplified pressure vessel theory deduces, the hoop stress required to balance a cross tank section is much higher than this internal radial stress:

$$\sigma_{\theta\theta} \approx p\frac{D_{int}}{2e} \tag{25}$$

which means that $\sigma_{\theta\theta}$ would be approximately 455 times larger than σ_{rr} in this case. Concerning axial stresses σ_{zz}, as long as there is no vertical restriction, they will be caused by the own weight of the structure and by the torsion phenomenon of large axial temperature gradients [40, 41]. Similarly to σ_{rr}, the effect of σ_{zz} in the equivalent stress is very low as it was also concluded in [23]. That is why, though the three-dimensional thermoelastic model is evaluating all components of the stress tensor, only the hoop stress is highlighted.

The stress state at the beginning of the simulation is only due to fluid hydrostatic pressure and gravel active load because homogenous heating from ambient temperature to T_{cold} does not produce any perceptible stress. A hoop stress directly proportional to this pressure, which increases linearly from top

17

to bottom, is developed. As it is depicted in Figure 6 (c) at "9 am", $\sigma_{\theta\theta}$ profile is not linear owing to the variable wall thickness.

In the course of the first heating (from "9 am" to "+ 9 h"), when the fluid sets the highest stratification and there is still no particle settlement, a wave of hot-compressive/cold-tensile hoop stress moves together with the temperature gradient. Once the gradient has passed a specific height, the circumferential stress returns to its previous value in that point. The apparent remaining stress increment that can be seen in the graph is only due to the reduction in the yield strength with high temperatures, the absolute hoop stress does get its old value.

During discharge (from "+ 12 h" to "+ 18 h"), radial contraction is restrained down to the new radius of the filler material. That is, as it is cooled, filler pressure rises and accordingly the thermal hoop stress. In this case, the solid pressure never exceeds the passive pressure of Equation 22, hence there is no plastic deformation of the particulate solid, i.e. it is always responding rigidly. This means that filler pressure rise and thermal hoop stress are proportional to the temperature drop in time. Therefore, after discharge, an almost constant thermal stress is observed between 4 and 8 m, in which ΔT is nearly 100 ºC. This thermal hoop stress is added to the elastic stress the structure has at the beginning of the simulation. Consequently, the maximum stress relative to the yield strength the structure must withstand is almost 0.6 at 3.4 m from the ground as a combination of thickness, maximum temperature variation in time and high active pressure. Being $\sigma_{eq} < \sigma_y$, the structure is always working within the elastic regime.

From this 1st cycle on, the structure relaxes every charging process (see Figure 6 (d)). The thermal stress in a section is completely removed as soon as the temperature in that section reaches its historical maximum, at which the maximum radius of the bed was established. However, while discharge takes place, it is stressed from top to bottom following the temperature decrease and its tendency to contract.

3.3. Validation

The numerical solution for bed temperature during the second-day charging process, when the axial temperature gradient is still fairly large, is shown in Figure 7. The results are compared with the bed temperature measurements collected by thermocouples installed in the storage unit of Solar One during May 18, 1983 [38]. Good agreement between experimental and numerical results is observed.
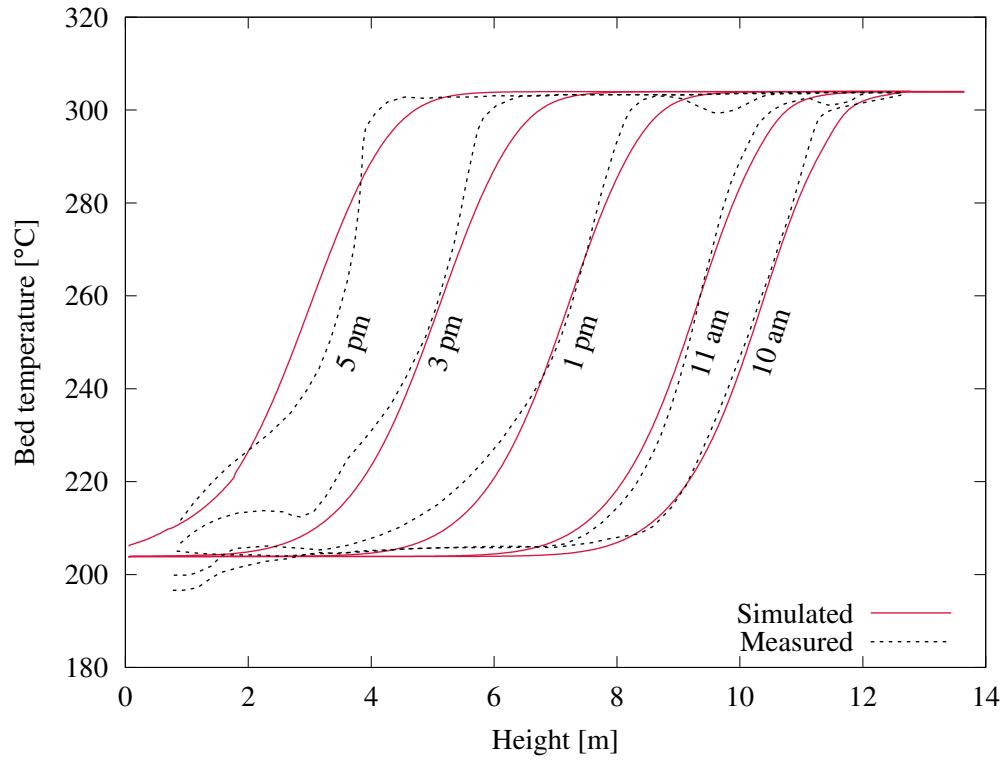
18

Figure 7: Temperature maps of Solar One bed during the second-day charge. Numerical simulation results (solid lines) and measures on May 18, 1983 [38] (dashed lines).
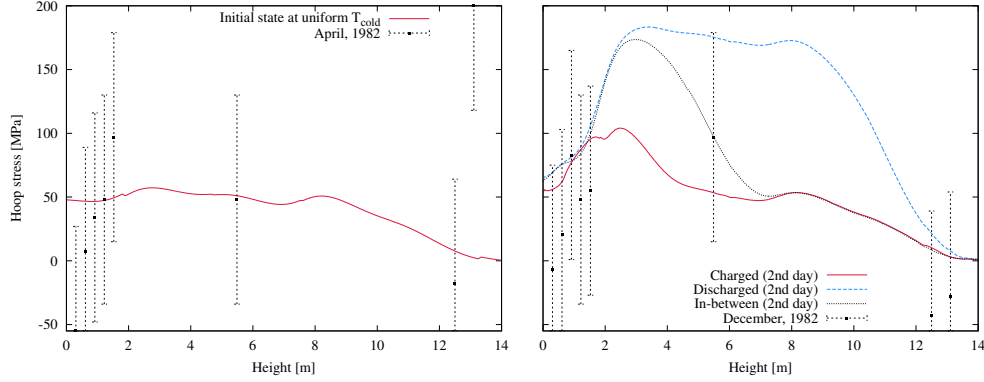
Figure 8: Hoop stress in Solar One thermocline tank. Characteristic simulation results (lines) and measured data [7] (dots).

Nevertheless, whereas curves from the simulation show a similar gradient when reaching both temperature extremes, real profiles have a far sharper change of temperature in the hot part than in the cold part. This is probably explained by the cycles preceding the measures. Focusing on the hot part of the thermocline, the colder the temperature reached at the top while discharging, the sharper the gradient of temperature in the following charging and thenceforth. Similarly for the cold part. Thus, it seems that before May 18, 1983, the cut-off temperature for discharge had been considerably lower than the one imposed in the simulation, 300 °C.

Regarding the structural analysis, the only measured stresses from [7] have been used, even though according to the original authors, some of them were inconsistent with the problem physics and there was significant uncertainty. Measurement errors of around 56 MPa to 142 MPa were possible. In this paper, an intermediate error of 82 MPa, mentioned in [7], has been considered.

Measurements and hoop stress resulting from the model are plotted in Figure 8. Readings from April 1982, just prior to heating for the first time the thermal storage unit, are compared with the hoop stress at the beginning of the simulation. The data recorded after a few operating cycles in December 1982 are presented with the main results from the 2nd day because there is no information about the specific time when these stresses were measured. Numerical results of both cases come close to the recorded stress variability, and are within the range of uncertainty of the most reliable measures (the

20

second, third and fourth point starting from the base according to [7]). The differences at the bottom part are likely to be due to the boundary condition, which in the simulation is only restricting vertical displacement, but not axial bending nor radial expansion.

More measured stresses in June 1984 revealed that an averaged hoop stress of 180 MPa was placed in the 0.6096 m to 1.219 m region. The magnitude is equal to the maximum stresses obtained from the simulation, but they are located between 3 m and 3.7 m. This suggests that Solar One tank would have been charged more than in the simulation, reaching higher temperatures near the ground. If there had been a similar heating in the simulation, the larger thermal stresses, consequence of the temperature variation, would have extended closer to the bottom.

Consequently, the whole numerical platform developed, including modeling and linking of all thermocline storage elements, agrees consistently with real temperatures and hoop stresses of packed-bed thermal storage tanks.

4. Definition of the cases

Having implemented and validated the simulation platform, and having understood the mechanical response of thermocline tanks, it is time to analyze their behaviour facing a real up-to-date situation. For this purpose, two CSP plants, which are currently working with a two-tank molten salt storage, have been selected as scenes to test different thermocline tank configurations. On the one hand, there is the Andasol-1 thermosolar plant based on a parabolic-through technology with a temperature difference of 100 °C. On the other hand, there is the Gemasolar plant which has a central tower receiver that raises the HTF temperature by 275 °C. The reference case related to the former will be referred to as $\mathcal{A}$, whereas the one placed in the latter will be referred to as $\mathcal{G}$. Here below, the particular specifications of case $\mathcal{A}$ [42, 25, 43] (those belonging to the tank have been extracted from the hot tank of the real plant):

- Plant configuration: $\dot{W}_{\mathrm{EG}} = 50$ MW, $A_{\mathrm{SF}} = 510\,120$ m^2, $T_{cold} = 290$ °C, $T_{hot} = 390$ °C, $\eta_{\mathrm{PB}} = 0.38$, $\eta_{\mathrm{SF}} = 0.7$.

- Location: Aldeire (Granada, Spain). The meteorological data for the 8760 hours in a reference year have been generated by [44] (irradiation) and [45] (ambient temperature, wind, humidity, pressure). Essential data are given in Table 2.

21

- Geometry: $h_{tank} = 14$ m, $h_{bed} = 13.16$ m. The tank appropriate diameter is determined in the next section.

- Materials: A387 grade 91 alloy steel for the tank shell, 0.4 m of Spintex342G100 for tank insulation and 0.001 m of aluminum as tank cover.

- Foundation thicknesses: 0.006 m of slip plate, 0.006 m of dry sand, 0.420 m of foam-glass, 0.060 m of hard fire-brick, 0.360 m of insulating fire brick, 0.450 m of heavy weight concrete and 9 m of soil.

Likewise, after consulting [46, 47, 48], the characteristics of case $\mathcal{G}$ can be listed:

- Plant configuration: $\dot{W}_{\mathrm{EG}} = 19.9$ MW, $A_{\mathrm{SF}} = 306{,}658$ m^2, $T_{cold} = 290$ °C, $T_{hot} = 565$ °C, $\eta_{\mathrm{PB}} = 0.40$, $\eta_{\mathrm{SF}} = 0.42$.

- Location: Fuentes de Andalucía (Sevilla, Spain). All the meteorological data are from [45] and are summarized in Table 2.

- Geometry: $h_{tank} = 11.2$ m, $h_{bed} = 10.5$ m. The tank appropriate diameter is determined in the next section.

- Materials: N06022 nickel-chromium-molybdenum alloy for the tank shell, 0.4 m of fiberglass for tank insulation, and 0.001 m of aluminum as tank cover. Although the metal used in the hot tank of the real plant is an A240 grade 347 stainless steel, preliminary studies revealed that its yield strength ($\sim$140 MPa at 427.5 °C) was too low for proposed thermocline storage. Therefore, following [37], the nickel alloy was chosen owing to its similar physical properties and to its higher resistance at moderate temperatures.

- Foundation thicknesses: 0.006 m of slip plate, 0.165 m of firebrick, 0.3 m of foam-glass, 0.23 m of insulating concrete, 0.61 m of concrete slab and 9 m of soil.

Vertical walls of both tanks have been divided uniformly into six plates with the thicknesses of the current Andasol hot tank. According to [25, 26], they are, from bottom to top: 0.039 m, 0.032 m, 0.0255 m, 0.0185 m, 0.0115 m and 0.01 m.

Solar salt (60% NaNO$_3$ + 40% KNO$_3$) has been chosen as HTF for the reference cases, as it is employed in the original two-tank subsystems. Regarding the fillerbed, a mixture of two solids of differing particle diameter, e.g. rock and sand, is preferred because it allows closer packing and, thus, less fluid is required. To prevent sand from entering in the piping system, there is a layer with only rocks surrounding the two manifolds. Therefore, similarly to [7, 5, 6] designs, the fillerbed has been stratified in four layers of quartzite rock and silica sand. At the bottom, 1% of the bed height is filled with sand. Above the sand layer and at the top, enclosing the manifolds, there are rock-only regions with a height of $0.08h_{bed}$. Sandwiched between these two layers is the mixture of rock and sand. Their porosity and effective particle diameter are just like in the validation case. Moreover, air at atmospheric pressure is placed in the ullage space. Table 1 contains the physical properties of this gravel and the remaining materials.

Another common feature for both cases is the stop/restart criteria for charge and discharge processes. They have been defined respectively by the following temperature increments: $\Delta T_{CO} = 15$ °C and $\Delta T_R = 10$ °C. The cut-off temperature takes into account the acceptable range of temperature entering into the solar field and power block [49, 50]. Besides this, the period of plant operation has been the same in the simulations too. May is left for reaching the periodic cyclic state, independent of the initial conditions of the first cycle. After that, the daily service during June, July and August is used for the result collection and processing.

Finally, considering their height, $\mathcal{A}$'s tank has been axially discretized in 800 control volumes, whereas $\mathcal{G}$'s has needed 638. After a mesh refinement study, it was found that there were less than 1% and 2% difference in the numerical results with refined meshes of double number of control volumes concerning case $\mathcal{A}$ and $\mathcal{G}$, respectively.

Simulating this period by the wall three-dimensional thermoelastic solver has a very high computational cost to carry out a suitable parametric analysis. It has been proved that fairly similar strain-stress results can be obtained with a one-dimensional (z) model analogous to that used for pressure vessels. It just considers the principal stresses: σ_{rr} takes $p_f(\tilde{z})$ value, σ_{zz} derives from the structure's own weight only (no bending effect), and $\sigma_{\theta\theta}$ is evaluated via Equation 25. The boundary conditions are strictly maintained. In Solar One validation exercise, height-averaged discrepancies of the simplified model compared with the general 3D theory were less than 7% while the difference in the maximum stress, located at $z = 3.4$ m, was ∼3%. By using
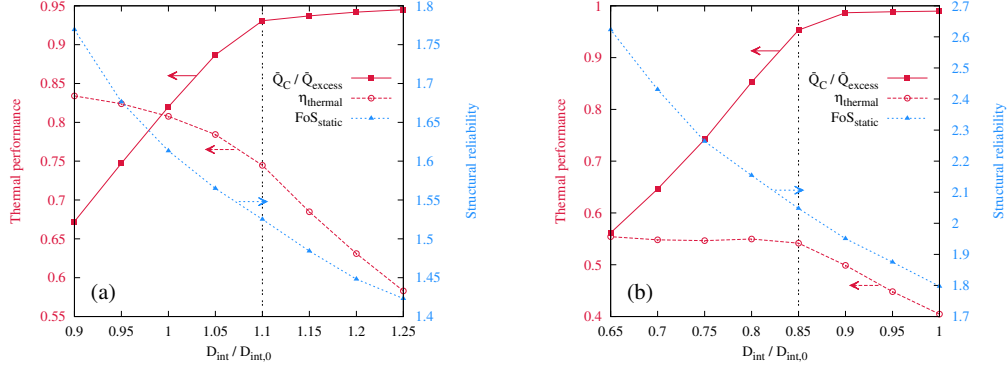
23

Figure 9: Change on some $\mathcal{A}$ (a) and $\mathcal{G}$ (b) operating conditions due to tank diameter. Thermal energy stored relative to the excess energy from the solar field, thermal efficiency and static factor of safety.

this model for the parametric study, a good approximation of tank stress response and its trends over normal operating periods will be assessed.

4.1. Definition of the tank volume

The authors of [39] noticed that, in the Andasol plant, the packed-bed tank should be larger than the hot two-tank so as to gain the thermal energy lost by thermocline degradation.

To determine the tank volume, only the radius will change, keeping the original height previously mentioned fixed. In the course of the study, the diameter of the real two-tank subsystem is taken as a reference. In the Andasol plant, the hot tank diameter, $D_{int,0}$, is 38 m, whereas in Gemasolar it is 23 m. The optimum volume will have to balance safety, thermal performance and cost during the three-month period previously defined. The first requirement is measured by the most conservative structural factor of safety (see Equation 23). The second, by the capability to store the excess thermal energy of the plant, i.e. the part of the solar energy that is not needed in the power block,

$$\dot{Q}_{excess} = \dot{Q}_{\text{SF}} - \dot{Q}_{\text{PB}} \tag{26}$$

For the stored energy, enthalpy difference is evaluated at each portion of the fluid and solid discretized domains. The thermal energy stored over the

24

time step moving from iteration n to $n+1$ results in:

$$Q_{C,f}^{n+1} = \sum_i \rho_f \epsilon_i V_i C_{p,f} \left(T_{i,f}^{n+1} - T_{i,f}^n \right) \tag{27}$$

$$Q_{C,s}^{n+1} = \sum_i \left(\sum_j \rho_s V_{i,j} C_{p,s} \left(T_{i,j}^{n+1} - T_{i,j}^n \right) \right) \tag{28}$$

$$Q_C^{n+1} = Q_{C,f}^{n+1} + Q_{C,s}^{n+1} \tag{29}$$

The day stored heat is obtained by adding all stored energies throughout a charge process. With this, a three-month operating period will be summarized by means of the daily averaged energies as $\bar{Q}_C / \bar{Q}_{excess}$.

The economic requirement is outlined thanks to thermal efficiency. It is evaluated as the thermal energy stored in the tank divided by its ideal storage capacity,

$$\eta_{th} = \frac{\bar{Q}_C}{Q_{storable}} \tag{30}$$

where $Q_{storable}$ is calculated as the heat needed to raise the temperature of the entire tank from T_{cold} to T_{hot}.

How do these variables behave facing a change in volume? If the tank is too small, its storage capacity is small and it will be unable to accumulate all the plant surplus solar energy ($\bar{Q}_C / \bar{Q}_{excess}$ less than one). By contrast, if it is overdimensioned, it will store this energy ($\bar{Q}_C / \bar{Q}_{excess}$ close to one), but it will not be using all its height, since there is not enough energy to charge it completely. This means a drop in η_{th} and a tendency of the thermal gradient to spread across a big part of the height (high thermal degradation, low stratification). In other words, there will be an unneeded stock of salt and rocks in the storage system. In addition, from equations 15 and 16 it is known that inner pressure will not change because it only depends on the depth $\tilde{z}$. Even so, as can be observed from Equation 25, the larger the radius, the higher the stress in the tank shell, i.e. the less FoS.

An overview of the simulations is presented in Figure 9, where all three requirements of the optimum volume are plotted. The trend is pretty similar in both cases $\mathcal{A}$ and $\mathcal{G}$. At first, when the volume is not big enough to accommodate all the thermal energy, the tank is fully heated in every charge process, which results in a steady high efficiency. When raising the radius, there is a particular point beyond which the tank is already storing almost all the energetic surplus, and the efficiency starts falling due to growing non-used

bed height. In terms of structural reliability, the factor of safety decreases steadily with the radius as expected, but never arising material yielding.

It turns out that the original volume of case $\mathcal{A}$ is evidently too small for the magnitudes of its plant, while it is oversized for case $\mathcal{G}$. Observing Figure 9 (b), the optimum diameter of $\mathcal{G}$ should be between $0.85D_{int,0}$ and $0.9D_{int,0}$. Having prioritized thermal efficiency, $0.85D_{int,0}$ is chosen for the reference tank $\mathcal{G}$. As for case $\mathcal{A}$, efficiency has a perceptible stagnation beyond $D_{int} = 1.1D_{int,0}$. Accordingly, this diameter is selected for $\mathcal{A}$, as it also lies on the smooth decline of the efficiency curve. In Table 3, there are the masses filling each sized tank as well as their storage capacity.

4.2. Definition of the parameters

The parametric analysis has been carried out in order to distinguish critical factors that might compromise the structural integrity of a thermocline packed bed tank and, at the same time, to assess their effects from a thermal point of view. Sized tanks of section 4.1 are treated as base cases (code B). Five different parameters of these cases have been altered so as to generate the new prototypes:

1. Bed aspect ratio (h_{bed}/D_{int}). Two different geometric configurations have been tested: one taller than the reference tank (code AR1) and another shorter (AR2); both with the same volume and the same quantities of salt, rock and sand. First, AR1 is defined to have a height of 16 m (the maximum allowed according to [6]), hence the corresponding diameter can be found in order to preserve the volume. The inverse of the change in aspect ratio of AR1 is then applied to sketch AR2. The diameter is restricted to a maximum of 48 m underlined in [5]. The final geometry of each case is presented in Table 4. The new configurations are made up of plates of the same height and thickness as the reference case. The taller case uses the thinnest plate of 0.01 m to reach 16 m high. AR2 simply places the same plates from bottom to top reaching the new height. The discretization of these prototypes has been adapted to keep the same Δz of the base cases.
2. Cut-off temperatures. One case (CO1) has wider admissible temperature intervals for both charge and discharge processes: $\Delta T_{CO} = 25$ ºC. The opposite one (CO2) has narrower intervals: $\Delta T_{CO} = 5$ ºC. ΔT_R is kept unchanged.
3. Season. While the base case works from May to August, this case (S1) runs from November to February.

4. Location. The location of Upington, in South Africa, has been selected to place the reference plants during summer (L1) and winter (L2).
5. Wall thickness. A new tank with 50% thicker thicknesses of the metal tank shell has been tested (T1).

5. Results and discussion

Tables 5 and 6 show the averaged quantitative results obtained from the simulation of the different cases considered, after the periodic state has been reached. Firstly, the focus will be on the main differences between base cases $\mathcal{A}$ and $\mathcal{G}$ and then on the effect of each parameter. But before this, it is necessary to explain some new variables attached in the tables:

- For evaluating the power generating potential of the energy delivered by the thermal storage, the exergy global balance of the HTF is calculated in the following manner (see Figure 2):

$$\dot{B}_D = \dot{m}_D C_{p,f} \left(T_D^{out} - T_{\mathrm{PB}}^{out} - T_{ref} \ln \frac{T_D^{out}}{T_{\mathrm{PB}}^{out}} \right) \qquad (31)$$

where T_{ref} is the temperature corresponding to dead state, which in this work has been taken as 45 °C due to being a reasonable value for the temperature at which vapour is condensed in the power generation block.

- Stand-by periods result from two types of imbalance: thermal energy in excess (the tank has been fully charged and there is still radiation), and lacking thermal energy (the tank has been already discharged and there is no radiation). The former forces to throw part of the available solar energy and the latter to resort to an alternative heat source, i.e. fossil fuels, to cover the thermal demand of the power block. This scarcity is presented in the tables relative to the total thermal energy requested by the generation subsystem to have firm capacity ($\bar{Q}_{lacking}/\bar{Q}_{\mathrm{PB}}$).

- The thermocline thickness h_{th} is measured as another indicator of thermal performance. Its formulation is similar to that proposed by [49]:

$$h_{th} = \begin{cases} \frac{h\left(T_{hot,c}\right) \Delta T_{th}}{T_{hot,c} - T_{bottom}}, & T_{bottom} > T_{cold,c} \\ \frac{\left(h_{bed} - h\left(T_{cold,c}\right)\right) \Delta T_{th}}{T_{top} - T_{cold,c}}, & T_{top} < T_{hot,c} \\ h\left(T_{hot,c}\right) - h\left(T_{cold,c}\right), & \text{elsewhere} \end{cases} \qquad (32)$$
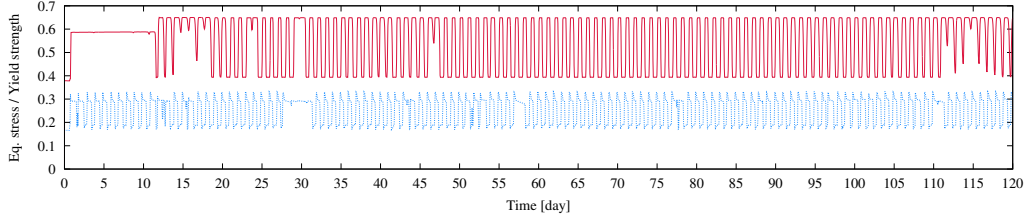
Figure 10: Total load history of base cases (B): tank $\mathcal{A}$ at $h = 7$ m (solid line) and tank $\mathcal{G}$ at $h = 6$ m (dashed line).

where $T_{hot,c}$ and $T_{cold,c}$ are the critical cold and hot temperatures for delimiting the thermocline thickness, respectively; and $\Delta T_{th} = T_{hot,c} - T_{cold,c}$. In the present study, $T_{hot,c}$ has been chosen to be $T_{hot} - 15$ and $T_{cold,c}$ to be $T_{cold} + 15$.

5.1. $\mathcal{A}$ versus $\mathcal{G}$

Observing the first row of tables 5 and 6, one may notice that solar thermal energy received throughout a day in $\mathcal{A}$ is significantly greater than that in $\mathcal{G}$. The causes are basically three: a larger collector's area (1.66 times larger in $\mathcal{A}$), a greater collecting efficiency (1.67 times), and a greater solar irradiation (1.13 times). Unfortunately, this total source represents only 93% and 79% of the thermal energy required by $\mathcal{A}$ and $\mathcal{G}$ power blocks, respectively. Taking into account this limitation, it should be concluded that the sizing of base storage tanks was properly done, since plant lacking energy agrees with these ideal values. In fact, both tanks keep about 95% of the available surplus solar energy. In terms of the portion of solar energy not directly sent to generation and hence storable, it is almost equal in both cases owing to the similarity of the collector's area solar multiple: ∼2.6 in $\mathcal{A}$ and ∼2.7 in $\mathcal{G}$.

If attention is paid to cycle times, no further conclusion can be drawn. The lacking energy previously stated can also be seen in the number of hours $\mathcal{G}$ tank is in stand-by with no deliverable energy, 6.3 h. Increasing receiver area and, consequently, enlarging the storage tank, would reduce this idle time, as $\mathcal{A}$ does with only 2.4 h.

Another remarkable figure is thermal efficiency, which is considerably poorer in case $\mathcal{G}$. The fact is that $\mathcal{G}$'s thermal performance will never be as good as $\mathcal{A}$'s, provided that outlet temperature tolerances are the same in both cases ($\Delta T_{CO} = 15$ °C). With the same tolerance, the thermal gradient will

28

be the same, but, since the temperature difference $T_{hot} - T_{cold}$ to overcome is larger in $\mathcal{G}$, the gradient region will be eventually wider there. This is clearly shown in Figure 12. The result is that the tank $\mathcal{A}$ accumulates three-fourths of its ideal capacity, whereas $\mathcal{G}$ just half. These ideal capacities are almost equivalent to equally sized two-tank systems, because the heat capacity ($\rho_f C_{p,f}$) of salt and quartzite are pretty similar.

In all cases, thermal losses are very low (less than 1% of the energy delivered to the power block by the TES), which is an indication of having sufficient thermal insulation.

In terms of stress on the tank shell, the first thing worth mentioning is that both factors of safety are greater than one. According to simulations, it implies that the metal structure is never subjected to plastic deformation nor, as a result, to ratcheting. In addition, they are within the safety limit of 1.5 against yield failure recommended by [51]. Nevertheless, given the approximations made –regarding the particulate medium mechanics or the physical properties– more conservative factors would be preferable for a commercial design.

The disparity between static and dynamic factors of safety is simply due to the averaged minimum stress, which is only influencing the latter (see Equation 24): the higher it is, the less stress oscillation, and the higher $FoS_{dynamic}$. The equivalent stress history presented in Figure 10 shows that there has not been any particular day in which the stress was higher than usual. That is why there is no big effect of averaging the daily maximum and minimum stresses and it seems more reliable to focus on FoS_{static}, at least in these cases.

Comparing the safety factors of $\mathcal{A}$ and $\mathcal{G}$, an unexpected fact is revealed: $\mathcal{G}$ vessel is safer than $\mathcal{A}$ vessel, although temperature decline in $\mathcal{G}$ is almost three times larger than that in $\mathcal{A}$. To understand it, Figure 11 should be examined first. The graph shows the maximum and minimum stresses reached on an average day, when the tank is fully discharged and fully charged, respectively (sudden changes in the profiles are due to the one-dimensional elastic solver). As can be seen, maximum stresses are all roughly 0.2 points above the minimum ones, while in Solar One case there was a 0.4 point rise during discharge, as a proportional result of the 100 ºC temperature drop. The explanation is that in these new examples the maximum lateral resistance of the bulk solid, i.e. the passive pressure, has been reached, unlike what happened in the Solar One simulation.

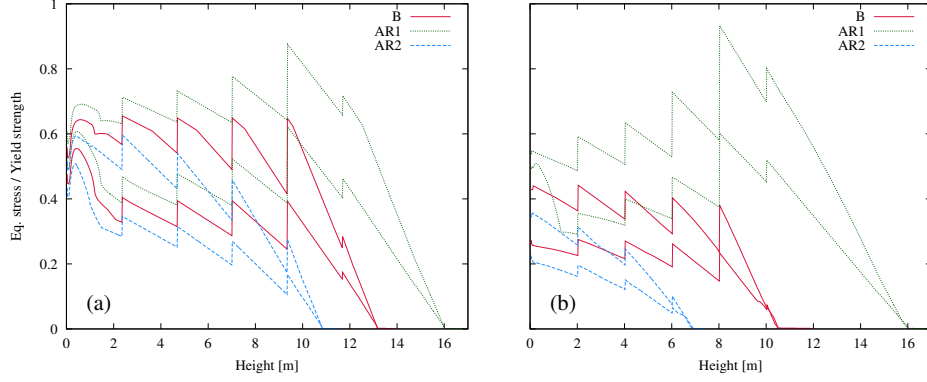But, why are these configurations reaching passive pressure if Solar One

Figure 11: Wall equivalent stress for base cases and their aspect ratio variations on July 9. Maximum stresses belong to discharged state and minimum stresses to charged state. Case $\mathcal{A}$ (a) and $\mathcal{G}$ (b).

did not? The key is in the fluid density. The oil used in Solar One was four times lighter than quartzite gravel in such a way that solid pressure represents four-tenths of the total inner pressure (see Equation 14). By contrast, in the reference tanks the fluid is only 1.4 times lighter than the gravel. Fluid and rock densities are similar, hence rocks "float more" and provide just one-tenth of the total inner pressure (see ρ_{buo} of Equation 18). It is known that passive pressure multiplies the active one by nine (due to the angle of internal friction), but if this latter hardly represents a minor part of the total, then the difference between total pressure with active response and total pressure with passive response will be minimum. Therefore, having a denser HTF ends up being beneficial from a structural point of view, because it reduces the rock pressure and prevents the total temperature difference effect, which would lead to considerably more dangerous stresses.

The increase in hoop stresses during discharge is not proportional to the temperature change, but is just determined by the bed passive pressure. Thus, having a similar distribution of internal substance pressure, only tank size and thicknesses might create the difference between both cases $\mathcal{A}$ and $\mathcal{G}$. The tank shape discussion of the next section clarifies their influence over mechanical performance.

5.2. Effect of aspect ratio: AR1-AR2

Concerning thermal performance, the results agree well with the idea expounded on [5]. The taller the tank, the better. Since the space occupied

by the thermocline gradient is the same (for a given temperature difference and a process outlet threshold), the more height, the more proportion of the volume can be warmed to T_{hot}. In case $\mathcal{G}$, the aspect ratio variations are more pronounced than in $\mathcal{A}$, and the differences in operation are more noticeable. Thermocline thickness falls from $0.42h_{bed}$ in the reference tank to $0.38h_{bed}$ in the higher modification (AR1), which allows it to collect 4% more surplus energy. The shorter tank (AR2) instead, can only collect 78% of this energy because of the relatively thicker thermocline. This constraint is forcing processes to extend more often to cut-off point (outlet temperatures start to decay earlier).

In this manner, in spite of having equal storage capacity (same amount of fluid and gravel), the higher prototype is more efficient thermally and can accumulate more energy. In other words, if the vessel geometry is stretched, its volume can be reduced without altering the final storage capacity. This is particularly important as long as $T_{hot} - T_{cold}$ increases: with 100 ºC like in $\mathcal{A}$, a bed 10.82 m tall leads to efficiencies close to 80%, whereas with 275 ºC, a bed height of 16 m is needed to at least arise a 60%.

Wall equivalent stress plotted in Figure 11 reveals its strong dependence on varying plate thickness. It has already been mentioned that fluid and rock pressure only depends on the depth measured from the bed surface ($\tilde{z}$). However, hoop stress is different at a common depth for all three modifications. It is a consequence of the traction developed on the wall under an inner pressure, which is proportional to D_{int}/e, as can be seen in Equation 25. Although AR1 has a smaller diameter, the plate thickness for a certain depth is much smaller, resulting in a higher factor D_{int}/e and hoop stress. The opposite happens with AR2; the diameter is larger but the thicknesses are much larger, so stress eventually falls.

In the end, the higher tank seems equally preferable. Although the metal shell should be thicker in order to be structurally reliable, the economic investment could be balanced by the fluid and gravel savings, because it is more thermally efficient.

And this explains the difference aforementioned between base cases $\mathcal{A}$ and $\mathcal{G}$. Though the steel's yield strength is higher than the nickel alloy's (see Table 1), the relative stresses presented in Figure 11 are still higher in $\mathcal{A}$. The fact is that absolute stresses are much larger in $\mathcal{A}$ than in $\mathcal{G}$ because the factor D_{int}/e is much larger too.
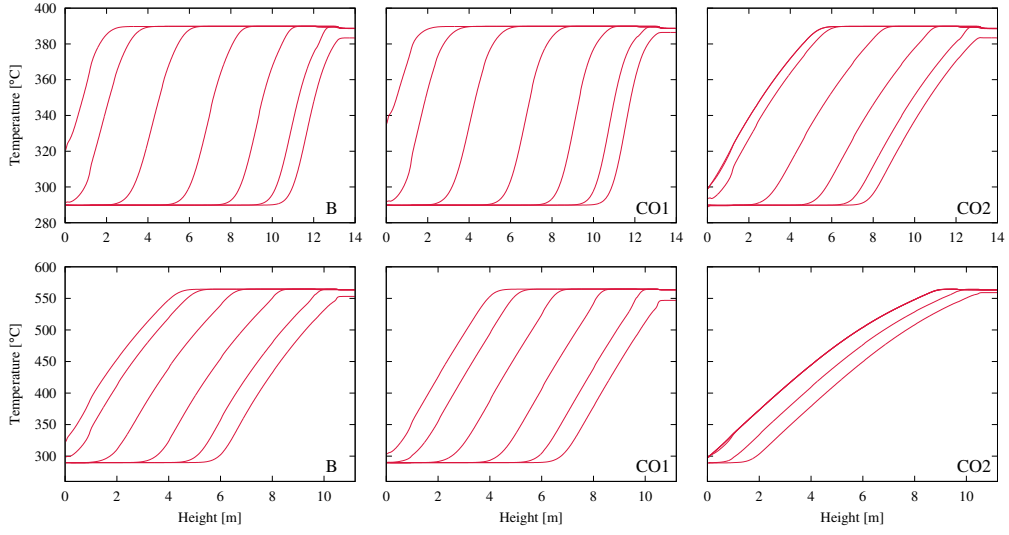
Figure 12: Wall temperature maps throughout charge on July 9. The curves are separated by a 2-hour interval and their chronological order is from right to left. $\mathcal{A}$ charge (top) lasted from 5 am to 5 pm and $\mathcal{G}$ (bottom) from 7 am to 5 pm.

5.3. Effect of cut-off temperatures: CO1-CO2

The base tank sizing procedure of subsection 4.1 is used for storing the maximum surplus solar energy. Both tanks were able to retain around 95% of that energy. As a result, raising the cut-off tolerance to 25 °C (CO1) is producing no remarkable difference as a TES. This strategy would be useful in a smaller tank. The tank would be able to accommodate the same heat with a higher efficiency, but having earlier-degrading outlet temperatures.

On the other hand, the reduced tolerance of $\Delta T_{CO} = 5$ °C negatively affects thermal operation. The thermocline height almost doubles, and so does the energy required from alternative sources. This thermal degradation is excessive in plant $\mathcal{G}$, as can also be identified in Figure 12.

The conclusion is that a tank cannot have steady design outgoing temperatures and a good thermal efficiency. The higher the tolerance in the temperatures entering the solar field and the power block, the better efficiency and the smaller tank needed.

There is another noteworthy feature in Figure 12. Although both charge and discharge processes are stopped when the block inlet temperature deviates ΔT_{CO} from its design temperature, it seems that this tolerance is higher in charging than in discharging. This is easily noticeable in $\mathcal{A}$ prototypes shown in Figure 12. Charge and power generation occur simultaneously (when there is sunlight). It means there is a cold HTF leaving the PB that is able to reduce the charge outlet temperature down to the cut-off temperature before entering the SF. By contrast, discharge and solar energy collection do not take place at the same time since discharge usually starts when there is no radiation. Therefore, mixing effect of Equation 6 hardly happens when there is discharge, and the temperature threshold is directly reflected inside the storage tank.

From a structural point of view, the impact of this parameter is negligible. Even so, due to the important thermal degradation of $\mathcal{G}$'s CO2 modification, the tank does not reach such big temperature changes nor such maximum stresses once the steady cycle has been set. Therefore, $FoS_{dynamic}$ increases.

5.4. Effect of season: S1

The most important parameter in the meteorological data is direct normal irradiance. From the averaged summary of Table 2, it is known that DNI approximately halves during winter in Granada as well as in Sevilla. Looking at the sixth row of tables 5 and 6, one deduces that both plants can only deliver about 40-45% electric energy from the solar power in winter, the
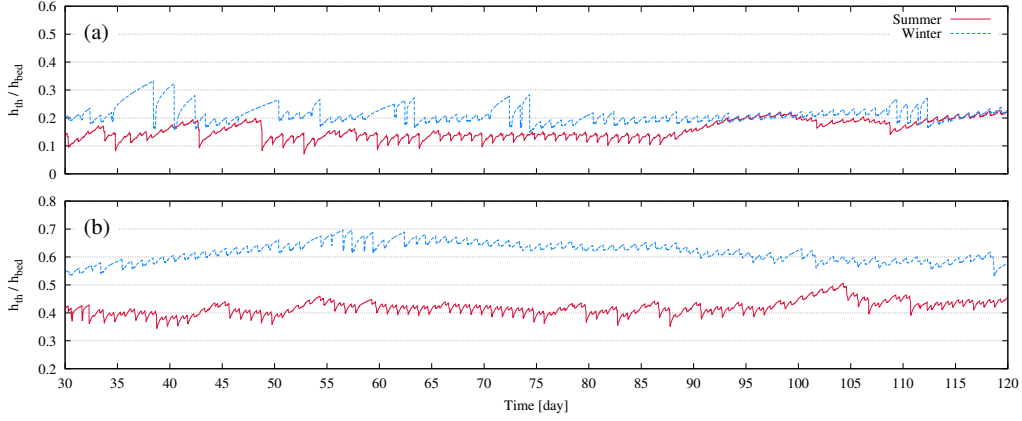
Figure 13: Thermocline height over a three-month period. $\mathcal{A}$ plant (a), located in Aldeire (Granada), and $\mathcal{G}$ plant (b), in Fuentes de Andalucía (Sevilla).

rest should be provided by other heat sources. Plant performance worsens considerably owing to seasonal variation in these two locations. For example, discharging time in $\mathcal{A}$ drops from 8.6 h during summer to 2.8 h in winter, while in $\mathcal{G}$ falls from 8 h to 4.2 h.

Now the focus will be specifically on the tank thermal efficiency and thermocline height. The former can be defined as the portion of the bed which is heated up to T_{hot} during charge. Therefore, it should be equivalent to consider the bed height (100%) minus the thermocline thickness. Nevertheless, in all the studied combinations, this value is higher than the actual efficiency (see Equation 30). This is a matter of weather, since the daily radiation is not always able to fill the tank until its limit. This issue is especially present in winter. Taking into account the thermocline thickness, $\mathcal{A}$'s tank can accumulate a 79% of what a zero-degradation thermocline TES would. But with the efficiency, this value is believed to be 16%. Having rare solar irradiance, the extreme thermal degradation is damped in this case by reaching the cutoff temperature at every discharge. This places the temperature oscillation only at the top of the tank, where stresses are not the highest. That is why $FoS_{dynamic}$ soars to 5.5 in $\mathcal{A}$.

In Figure 13 the temperature gradient length over the three-month period simulations is presented. Regardless the inherent fluctuations related to processes and stand-by periods, it can be seen that $\mathcal{A}$'s thermocline is pretty

34

stable and comparable throughout both periods summer and winter. The behaviour of $\mathcal{G}$ is fairly different. Initially, the storable energy is so scarce in winter that thermal degradation grows, and not until the end of second month (day 60) is it starting to decrease.

Therefore, cold seasons do affect the thermocline, increasing the degradation basically. But this degradation can be progressively lessened with increasing sunny days. Structurally, winter and the consequent degradation reduce the temperature decline during discharge, and hence the stresses.

5.5. Effect of location: L1-L2

Upington is definitely a fitting choice of CSP plant location because of its climate: sunny, warm and relatively constant throughout the year. Even so, and obtaining heat by the solar receiver similar to that of Spain, the tables prove that the defined TES does not adapt so well to this new place. Neither L1 nor L2 can even keep a 90% of the energy available for storage, and eventually the dependence on alternative heat sources to assure plant firm capacity increases.

Tables 2, 5 and 6 show that, even though the solar receiver collects a similar amount of solar energy, it takes far less time to do it. Solar radiation is shorter, but more intense than in Spain. This is reflected in the larger proportion of excess energy sent to storage, and in the shorter time devoted to charging. The resulting electrical power generated with warm fluid directly coming from the solar field falls, and the TES is asked to accumulate more thermal energy and retrieve it for a longer period.

This major role of TES within the plant would be satisfied by means of larger tanks, both in $\mathcal{A}$ and $\mathcal{G}$. With the current capacity the tanks are delivering the same exergy than in the reference cases: around 490 MWh over 8.4 h in $\mathcal{A}$ and around 180 MWh over 7.3 h in $\mathcal{G}$. But they are not enough for the longer periods with no radiation in Upington.

Concerning the stress-strain state of the walls, it can be seen that there is no variation since the inner materials and the work temperatures have not changed.

5.6. Effect of tank wall thickness: T1

The impact of the change in wall thickness is of minor relevance in terms of plant and storage performance. However, hoop stresses decrease approximately by a factor of 1.5, just what the thickness has risen. Thus, the results agree with the proportionality between $\sigma_{\theta\theta}$ and D_{int}/e already mentioned.

In order to arise a factor of safety against yield (and at the same time against thermal ratcheting) close to two, case $\mathcal{A}$ would need about 50% more wall thickness than a two-tank system, whereas $\mathcal{G}$ can be built with equal plates. As it has already been seen, it is not a matter of plant temperature difference, which is higher in $\mathcal{G}$ than in $\mathcal{A}$, but a matter of the larger size of tank $\mathcal{A}$.

6. Conclusions

A new validated numerical simulation platform for packed-bed thermocline energy storage tanks for CSP plants has been presented. It is able to dynamically solve and couple all its significant components so as to obtain the thermal and mechanical response of the subsystem over the plant's normal operation. The structure is calculated by means of the general thermoelastic theory for the tank wall and a rigid-perfectly plastic model with thermal expansion for the cohesionless bulk solid.

A broad thermo-mechanical parametric analysis is carried out in order to better understand whether the thermocline concept is a viable alternative for TES in CSP plants, regarding energetic effectiveness and structural reliability. It starts by sizing the thermocline storage system within two real commercial plants. The defined tanks work with solar salt as the HTF and a layered mixture of silica sand and quartzite rock as the filler material. A parabolic through plant with 50 MW$_e$ and 100 ºC of temperature difference leads to a 41.8×13.16 m (diameter×height) tank with 1010 MWh real storage capacity and 8.6 h delivering time. By contrast, a central tower plant with 19.9 MW$_e$ and 275 ºC of temperature difference gives rise to a 19.55×10.5 m tank with 348 MWh thermal energy deliverable along 8 h.

Their thermal efficiency differ greatly, from 75% in the former to 55% in the latter, due to the significance of gradient degradation in each case. Lower plant temperature difference as well as larger range of admissible temperatures in power block and solar field means a better storage performance. Other factors like vessel geometric aspect ratio or seasonal weather variation also affect the storage capacity. Generally, the thermal operation of the 275 ºC thermocline is considerably poor. Thus, it seems appropriate to consider improvements, like the multi-layered solid-PCM concept, for plants with a high temperature jump.

The numerical results show that material yielding, and hence thermal ratcheting, can be avoided in both cases with a factor of safety greater than

two. Key aspect of its design involves tank walls with proper thickness, but not more than 0.06 m, made of a high yield strength metal and a HTF with a density of the same order as that of the fillerbed. As observed, tank wall stress can be summarized by hoop stress, because the effect of radial stress, structure's own weight and high temperature gradient bending is negligible in the equivalent stress.

Acknowledgments

References

[1] A. Gil, M. Medrano, I. Martorell, A. Lázaro, P. Dolado, B. Zalba, L. F. Cabeza, State of the art on high temperature thermal energy storage for power generation. part 1—concepts, materials and modellization, Renewable and Sustainable Energy Reviews 14 (1) (2010) 31 – 55.

[2] G. J. Kolb, Evaluation of annual performance of 2-tank and thermocline thermal storage systems for trough plants, Journal of Solar Energy Engineering 133 (3) (2011) 031023 – 5.

[3] M. Liu, N. H. S. Tay, S. Bell, M. Belusko, R. Jacob, G. Will, W. Saman, F. Bruno, Review on concentrating solar power plants and new developments in high temperature thermal energy storage technologies, Renewable and Sustainable Energy Reviews 53 (2016) 1411 – 1432.

[4] D. A. Brosseau, P. F. Hlava, M. J. Kelly, Testing thermocline filler materials and molten salt heat transfer fluids for thermal energy storage systems used in parabolic trough solar power plants, Tech. rep., Sandia National Laboratories, Albuquerque, New Mexico, sAND2004-3207 (July 2004).

[5] Solar thermocline storage systems: Preliminary design study, Tech. rep., Electric Power Research Institute (EPRI), Palo Alto, CA, project 1019581 (June 2010).

[6] J. E. Pacheco, S. K. Showalter, W. J. Kolb, Development of a molten-salt thermocline thermal storage system for parabolic trough plants, Journal of Solar Energy Engineering - Transactions of the ASME 124 (2002) 153–159.

[7] S. E. Faas, L. R. Thorne, E. A. Fuchs, N. D. Gilbertsen, 10 mwe solar thermal central receiver pilot plant: Thermal storage subsystem evaluation – final report, Tech. rep., Sandia National Laboratories SAND86-8212 (1986).

[8] S. M. Flueckiger, Z. Yang, S. V. Garimella, An integrated thermal and mechanical investigation of molten-salt thermocline energy storage, Applied Energy 88 (6) (2011) 2098–2105.

[9] G. Zanganeh, A. Pedretti, S. Zavattoni, M. Barbato, A. Steinfeld, Packed-bed thermal storage for concentrated solar power – pilot-scale demonstration and industrial-scale design, Solar Energy 86 (10) (2012) 3084–3098.

[10] C. Mira-Hernández, S. M. Flueckiger, S. V. Garimella, Comparative analysis of single- and dual-media thermocline tanks for thermal energy storage in concentrating solar power plants, Journal of Solar Energy Engineering - Transactions of the ASME 137 (3) (2015) 031012–031012.

[11] B. M. Brown, M. N. Strasser, R. P. Selvam, Development of a structured thermocline thermal energy storage system, in: Proceedings of ASES, Vol. 74, 2012.

[12] F. Motte, S. L. Bugler-Lamb, Q. Falcoz, X. Py, Numerical study of a structured thermocline storage tank using vitrified waste as filler material, Energy Procedia 49 (2014) 935 – 944.

[13] M. Wu, M. Li, C. Xu, Y. He, W. Tao, The impact of concrete structure on the thermal performance of the dual-media thermocline thermal storage tank using concrete as the solid medium, Applied Energy 113 (2014) 1363–1371.

[14] Z. Yang, S. V. Garimella, Molten-salt thermal energy storage in thermoclines under different environmental boundary conditions, Applied Energy 87 (11) (2010) 3322 – 3329.

[15] M. Hänchen, S. Brückner, A. Steinfeld, High-temperature thermal storage using a packed bed of rocks – heat transfer analysis and experimental validation, Applied Thermal Engineering 31 (10) (2011) 1798 – 1806.

[16] J. T. V. Lew, P. Li, C. L. Chan, W. Karaki, J. Stephens, Analysis of heat storage and delivery of a thermocline tank having solid filler material, Journal of Solar Energy Engineering 133 (2) (2011) 021003 – 10.

[17] P. A. Galione, C. D. Pérez-Segarra, I. Rodríguez, A. Oliva, J. Rigola, Multi-layered solid-pcm thermocline thermal storage concept for CSP plants. numerical analysis and perspectives, Applied Energy 142 (2015) 337–351.

[18] C. J. Bunnell, J. C. Powell, Solar pilot plant, phase 1. preliminary design report. volume v. thermal storage subsystem. cdrl item 2, Tech. rep., Honeywell Energy Resources Center SAN-1109-8/7 (May 1977).

[19] R. W. Hallet, R. L. Gervais, Central receiver solar thermal power system, phase 1. cdrl item 2. pilot plant preliminary design report. volume 5. thermal storage subsystem, Tech. rep., McDonnell Douglas Astronautics Company SAN/1108-8/5 (October 1977).

[20] S. M. Flueckiger, Z. Yang, S. V. Garimella, Thermomechanical simulation of the solar one thermocline storage tank, Journal of Solar Energy Engineering 134.

[21] G. J. Kolb, G. Lee, P. Mijatovic, E. Valmianski, Thermal ratcheting analysis of advanced thermocline energy storage tanks, in: SolarPACES 2011, Granada, 2011.

[22] B. D. Iverson, S. J. Bauer, S. M. Flueckiger, Thermocline bed properties for deformation analysis, Journal of Solar Energy Engineering 136.

[23] I. González, O. Lehmkuhl, C. D. Pérez-Segarra, A. Oliva, Dynamic thermoelastic analysis of thermocline-like storage tanks, Energy Procedia 69 (2015) 850–859, international Conference on Concentrating Solar Power and Chemical Energy Systems, SolarPACES 2014.

[24] R. M. Damle, G. Colomer, O. Lehmkuhl, I. Rodriguez, Energy simulation of buildings with a modular object-oriented tool, in: ISES Solar World Congress, Kassel, 2011.

[25] I. Rodríguez, C. Pérez-Segarra, O. Lehmkuhl, A. Oliva, Modular object-oriented methodology for the resolution of molten salt storage tanks for CSP plants, Applied Energy 109 (2013) 402–414.

[26] S. Torras, C. D. Pérez-Segarra, I. Rodríguez, J. Rigola, A. Oliva, Parametric study of two-tank tes systems for CSP plants, Energy Procedia 69 (2015) 1049–1058, international Conference on Concentrating Solar Power and Chemical Energy Systems, SolarPACES 2014.

[27] N. Wakao, S. Kaguei, T. Funazkri, Effect of fluid dispersion coefficients on particle-to-fluid heat transfer coefficients in packed beds: Correlation of nusselt numbers, Chemical Engineering Science 34 (3) (1979) 325–336.

[28] H. Jasak, H. G. Weller, Application of the finite volume method and unstructured meshes to linear elasticity, International Journal for Numerical Methods in Engineering 48 (2000) 267–287.

[29] Željko Tuković, H. Jasak, Updated lagrangian finite volume solver for large deformation dynamic response of elastic body, Transactions of Famena 31 (2007) 1–18.

[30] J. G. Faber, F. H. Mead, Oscar Faber's Reinforced Concrete, Second Edition, Taylor & Francis, 1977.

[31] S. Helwany, Applied Soil Mechanics with ABAQUS Applications, John Wiley & Sons, 2007.

[32] S. Hansbo, Foundation Engineering, Developments in Geotechnical Engineering, Elsevier Science, 1994.

[33] A. Aysen, Soil Mechanics: Basic Concepts and Engineering Applications, Taylor & Francis, 2002.

[34] E. Zahavi, V. Torbilo, S. Press, Fatigue Design: Life Expectancy of Machine Parts, A Solomon press book, Taylor & Francis, 1996.

[35] R. G. Budynas, J. K. Nisbett, Shigley's Mechanical Engineering Design, McGraw-Hill Education, 2014.

[36] A. B. Zavoico, Solar power tower design basis document revision 0, Tech. rep., Sandia National Laboratories SAND2001-2100, San Francisco, CA (July 2001).

[37] American Society of Mechanical Engineers, An International Code - 2010 ASME Boiler & Pressure Vessel Code, Section II Part D - Properties (Customary) Materials (July 2007).

[38] 10 mwe solar thermal central receiver pilot plant mode 5 (test 1150) and mode 6 (test 1160) test report, Tech. rep., McDonnell Douglas Astronautics Company (November 1977).

[39] P. A. Galione, C. D. Pérez-Segarra, I. Rodríguez, S. Torras, J. Rigola, Multi-layered solid-pcm thermocline thermal storage for CSP. numerical evaluation of its application in a 50 {MWe} plant, Solar Energy 119 (2015) 134–150.

[40] S. Timoshenko, S. Woinowsky-Krieger, Theory of Plates and Shells, McGraw-Hill, 1959.

[41] I. Furuhashi, N. Kawasaki, N. Kasahara, Evaluation charts of thermal stresses in cylindrical vessels contained fluid, Journal of Computational Science and Technology 2 (2008) 547–558.

[42] The andasol project. workshop on thermal storage for trough power systems, Tech. rep., FLABEG Solar Int. GmbH, Solar Millennium AG.

[43] P. A. Galione, C. D. Pérez-Segarra, I. Rodríguez, S. Torras, J. Rigola, Numerical evaluation of multi-layered solid-pcm thermocline-like tanks as thermal energy storage systems for CSP applications, Energy Procedia 69 (2015) 832–841, international Conference on Concentrating Solar Power and Chemical Energy Systems, SolarPACES 2014.

[44] Radiación solar en andalucía, https://www.agenciaandaluzadelaenergia.es/Radiacion/radiacion1.php, accessed: 2015-09-07.

[45] S. Meteotest Fabrikstrasse 14, CH-3012 Bern, Meteonorm 4.0 (1999).

[46] B. Kelly, D. Kearney, Thermal storage commercial plant design study for a 2-tank indirect molten salt system, Tech. rep., National Renewable Energy Laboratory (NREL), final Report (July 2006).

[47] J. I. Burgaleta, S. Arias, , D. Ramirez, Gemasolar, the first tower thermosolar commercial plant with molten salt storage, in: SolarPACES 2011, Granada, 2011.

[48] Gemasolar plant in seville, spain, http://www.sener-power-process.com/ENERGIA/ProjectsI/gemasolar/en, accessed: 2015-09-21.

[49] C. Xu, Z. Wang, Y. He, X. Li, F. Bai, Sensitivity analysis of the numerical study on the thermal performance of a packed-bed molten salt thermocline thermal storage system, Applied Energy 92 (2012) 65–75.

[50] A. Modi, C. D. Pérez-Segarra, Thermocline thermal storage systems for concentrated solar power plants: One-dimensional numerical model and comparative analysis, Solar Energy 100 (2014) 84–93.

[51] An International Code - 2010 ASME Boiler & Pressure Vessel Code, Section VIII Rules for Construction of Pressure Vessels - Division 1, 2010.

Solar salt [36]	
ρ	1873.8
C_p	1501.5
k	$4.43 \times 10^{-4} + 1.98 \times 10^{-8}T$
μ_{visc}	$2.2714 \times 10^{-2} - 1.24 \times 10^{-4}T + 2.281 \times 10^{-7}T^2 - 1.474 \times 10^{-10}T^3$
Caloria HT-43 [7]	
ρ	692.4
C_p	2700
k	$1.25 \times 10^{-4} - 1.4 \times 10^{-7}T$
μ_{visc}	$132.73T^{-2.207}$
Sand and quartzite rock [7, 18]	
ρ	2643
C_p	1000.5
k	2.2
ϕ	30º
α	7.92×10^{-6}
Steel A537 Class 2 (from 477 K to 577 K) [37]	
ρ	7850
C_p	[512, 547]
k	[53.5, 49]
E	$[1.92 \times 10^{11}, 1.84 \times 10^{11}]$
ν	0.3
α	$[1.39 \times 10^{-5}, 1.49 \times 10^{-5}]$
σ_y	$[3.11 \times 10^8, 2.82 \times 10^8]$
$T_{\max}$	371
Steel A387 Grade 91 (from 563 K to 663 K) [37]	
ρ	7850
C_p	[541, 600]
k	[27.3, 27.8]
E	$[1.95 \times 10^{11}, 1.88 \times 10^{11}]$
ν	0.3
α	$[1.26 \times 10^{-5}, 1.32 \times 10^{-5}]$
σ_y	$[3.76 \times 10^8, 3.61 \times 10^8]$
$T_{\max}$	649
Nickel alloy N06022 (from 563 K to 838 K) [37]	
ρ	8691
C_p	[482, 532]
k	[15.2, 20.8]
E	$[1.91 \times 10^{11}, 1.75 \times 10^{11}]$
ν	0.3
α	$[1.32 \times 10^{-5}, 1.74 \times 10^{-5}]$
σ_y	$[2.16 \times 10^8, 1.88 \times 10^8]$
$T_{\max}$	1250

Table 1: Thermo-physical properties of the main materials used in the simulations. SI units.

Location	$T_{\min}$	$T_{\max}$	$\overline{DNI}$	$\bar{t}_{sun}$
Granada, Spain				
Summer	13.3	35.1	8222	14.3
Winter	2.1	21.1	3739	9.8
Sevilla, Spain				
Summer	13.3	35.1	7280	14.2
Winter	2.1	21.1	4148	9.7
Upington, RSA				
Summer	-0.1	25.9	6670	10.0
Winter	14.9	39.6	8455	12.7

Table 2: Location basic data. Here summer covers the months of June, July and August; and winter the months of December, January and February. T in [ºC], DNI in [Wh/m²day] and t_{sun} in [h].

	Case $\mathcal{A}$		Case $\mathcal{G}$	
$D_{int}/D_{int,0}$	1.1	1	0.85	1
Mass of filler material	35758	29552	6242	8639
Mass of confined fluid	8487	7014	1481	2050
Filler storage capacity	994	821	477	660
Fluid storage capacity	354	293	170	235
Total storage capacity	1348	1114	647	895

Table 3: Mass confined (ton) and storage capacity (MWh) of the reference tanks and those with the original two-tank molten salt storage radius, $D_{int,0}$.

	Case $\mathcal{A}$			Case $\mathcal{G}$		
	Base	AR1	AR2	Base	AR1	AR2
D_{int} [m]	41.8	37.91	46.09	19.55	15.84	24.13
h_{bed} [m]	13.16	16	10.82	10.5	16	6.89
AR	0.31	0.42	0.23	0.54	1.01	0.29

Table 4: Inner diameter, bed height and aspect ratio of the reference cases and their aspect ratio variations, AR1 and AR2.

Results	B	AR1	AR2	CO1	CO2	S1	L1	L2	T1
Energy from SF, $\bar{Q}_{SF}$ [MW h]	2936	2936	2936	2936	2936	1335	2382	3019	2936
Excess energy / Energy from SF, $\bar{Q}_{excess}/\bar{Q}_{SF}$ [%]	37	37	37	37	37	16	48	49	37
Stored energy / Excess energy, $\bar{Q}_C/\bar{Q}_{excess}$ [%]	93	93	93	93	74	100	89	69	93
Delivered energy / Stored energy, $\bar{Q}_D/\bar{Q}_C$ [%]	100	100	100	100	100	99	100	100	100
Delivered exergy, $\bar{B}_D$ [MW h]	485	486	484	487	386	100	491	490	485
Energy lacking / Energy needed, $\bar{Q}_{lacking}/\bar{Q}_{PB}$ [%]	8	8	8	8	15	58	28	17	8
Energy losses [MW h]	2.07	2.04	2.14	2.06	2.08	1.92	2.04	2.08	2.06
Charge time [h]	12.1	12.1	12.0	12.1	9.5	5.3	7.5	7.8	12.1
Discharge time [h]	8.6	8.6	8.5	8.6	6.7	2.8	8.4	8.4	8.6
Charged stand-by time [h]	1.0	0.9	1.0	0.9	3.5	0.0	0.9	3.0	1.0
Discharged stand-by time [h]	2.4	2.4	2.4	2.3	4.2	15.9	7.2	4.8	2.4
Time with $T_C^{out} < T_{cold} + 5$ [%]	97	97	97	97	100	100	96	97	97
Time with $T_D^{out} > T_{hot} - 5$ [%]	97	97	95	96	100	90	95	95	96
Thermal efficiency, η_{th} [%]	74	75	74	75	59	16	76	76	74
Thermocline height / Bed height, h_{th}/h_{bed} [%]	16	15	17	14	29	21	15	15	16
Static factor of security, FoS_{static}	1.5	1.1	1.7	1.5	1.5	1.5	1.5	1.5	2.2
Dynamic factor of security, $FoS_{dynamic}$	2.4	1.5	3.2	2.4	2.4	5.5	2.4	2.4	4.0

Table 5: Daily averaged performance results for each $\mathcal{A}$ configuration.

Results	B	AR1	AR2	CO1	CO2	S1	L1	L2	T1
Energy from SF, $\bar{Q}_{SF}$ [MW h]	938	938	938	938	938	534	859	1089	938
Excess energy / Energy from SF, $\bar{Q}_{excess}/\bar{Q}_{SF}$ [%]	39	39	40	39	39	32	46	45	39
Stored energy / Excess energy, $\bar{Q}_C/\bar{Q}_{excess}$ [%]	95	99	78	99	31	99	84	66	94
Delivered energy / Stored energy, $\bar{Q}_D/\bar{Q}_C$ [%]	100	100	100	100	98	100	100	100	100
Delivered exergy, $\bar{B}_D$ [MW h]	190	196	156	196	61	91	179	177	189
Energy lacking / Energy needed, $\bar{Q}_{lacking}/\bar{Q}_{PB}$ [%]	22	22	28	21	43	55	33	22	23
Energy losses [MW h]	0.96	1.02	0.96	0.93	1.00	0.93	0.97	0.96	0.96
Charge time [h]	9.1	9.7	7.3	9.7	3.6	5.5	7.0	7.3	9.1
Discharge time [h]	8.0	8.2	6.7	8.2	3.1	4.2	7.3	7.3	7.9
Charged stand-by time [h]	0.6	0.0	2.4	0.0	6.1	0.0	1.4	3.3	0.6
Discharged stand-by time [h]	6.3	6.1	7.6	6.1	11.2	14.3	8.4	6.1	6.4
Time with $T_C^{out} < T_{cold} + 5$ [%]	93	96	91	95	100	99	94	94	93
Time with $T_D^{out} > T_{hot} - 5$ [%]	93	95	90	91	100	91	93	93	93
Thermal efficiency, η_{th} [%]	54	56	45	56	18	26	51	50	54
Thermocline height / Bed height, h_{th}/h_{bed} [%]	42	38	55	40	75	62	45	44	43
Static factor of security, FoS_{static}	2.0	0.9	2.7	2.1	2.1	2.1	2.0	2.0	3.1
Dynamic factor of security, $FoS_{dynamic}$	3.4	0.9	5.2	3.5	3.7	4.2	3.4	3.5	5.6

Table 6: Daily averaged performance results for each $\mathcal{G}$ configuration.